Journal Pre-proof

Damage assessment method and key influencing factors for a typical rocket projectile during fragment cloud engagement

Chong Wang, Wenbo He, Ming Yang, Jinxiang Wang, Xulong Hao, Xiwen Chen, Chunjie Hao

PII: S2214-9147(26)00179-0

DOI: https://doi.org/10.1016/j.dt.2026.05.026

Reference: DT 2017

To appear in: *Defence Technology*

Received Date: 23 February 2026

Revised Date: 14 May 2026

Accepted Date: 31 May 2026

Please cite this article as: Wang C, He W, Yang M, Wang J, Hao X, Chen X, Hao C, Damage assessment method and key influencing factors for a typical rocket projectile during fragment cloud engagement, *Defence Technology*, https://doi.org/10.1016/j.dt.2026.05.026.

Damage assessment method and key influencing factors for a typical rocket projectile during fragment cloud engagement

Chong Wang[a], Wenbo He[a], Ming Yang[a*], Jinxiang Wang[a*], Xulong Hao[a], Xiwen Chen[a] Chunjie Hao[b]

[a]National Key Laboratory of Transient Physics, Nanjing University of Science and Technology, Nanjing, 210094, China

[b]Jinxi Defense Equipment Research Institute, Jinxi Industries Group, Taiyuan, 030027, China

[*]Corresponding author:Ming Yang,ym1991@njust.edu.cn;Jinxiang Wang,wjx@njust.edu.cn

[**] Corresponding author.

Damage assessment method and key influencing factors for a typical rocket projectile during fragment cloud engagement

Abstract: With the widespread application of active protection systems (APS) in tank warfare, accurately assessing the damage effects of interceptors against rocket projectiles has become a critical challenge for improving battlefield survivability. Here, a rapid and precise assessment method is proposed. First, partition the rocket into three functional zones—Fuse, Liner, and Charge—via target characteristic analysis. Multi-zone damage criteria are established, where failure thresholds for the fuse, liner, and charge are quantified via equivalent circuit analysis, geometric penetration constraints, and shock initiation simulation, respectively. Subsequently, a "Point-to-Surface Distance Method with an Enclosing Shell" is proposed to optimize the dynamic projectile-target intersection calculation, enhancing computational efficiency and avoiding unnecessary calculations, while ensuring geometric precision. Based on this framework, the coupling effects of intercept distance and attack angle on damage probability are systematically investigated using Monte Carlo Method. The results reveal a mechanism governing damage mode evolution. While the damage probability is saturated in the near-field, a significant non-linear behavior emerges with increasing intercept distance. At large attack angles, more fragments hit the charge, driving a transition in damage mode from "Loss of Warhead Power" to "Premature Detonation". This mechanism extends the 50% damage probability threshold from 1.3 m to 3.7 m, a nearly threefold increase. This methodology provides a scientific basis for the intercept parameter design of APS, with significant military value.

Keywords: Active protection system; Damage mode; Damage criterion; Damage assessment; Numerical simulation

1.Introduction

In modern military conflicts, the battlefield survivability of armored vehicles faces severe challenges. Anti-tank rockets have become a primary threat in ground combat scenarios owing to their low cost, high mobility, and potent damage effectiveness [1]. APS have been widely adopted in tank combat to counter this threat. These systems are capable of detecting incoming threats in real-time and launching interceptors to neutralize them, thereby enhancing the terminal defense capability of the armored platform [2,3]. The optimization of active protection strategies is heavily reliant on the precise assessment of interception effects. Research on target

damage assessment encompasses multiple facets, including the establishment of damage criteria, projectile-target intersection analysis, and damage probability calculation. However, due to the dynamic nature of the battlefield environment, the complexity of rocket structures, and the diversity of interception parameters, it is difficult for traditional evaluation methods to balance accuracy and efficiency [4]. In response, scholars have conducted extensive research, developing various computational models and methods.

In the study of target damage criteria, Wang et al [5]. proposed the "projection method" to address the 3D vulnerability analysis of complex system targets. This approach simplifies the problem into 2D equivalent models corresponding to different attack directions. Based on a physical equivalence method, it integrates multiple damage criteria, enabling rapid and simplified vulnerability assessment for complex targets. To further address the complex interrelationships among the internal components of the system, Goodrum et al. [6] presented a vulnerability analysis framework for shipboard distributed systems. Their approach integrates physical, logical, and operational architectures into a multiplex network model, enabling the identification of cascading failure risks due to functional interdependencies. To tackle the problem of correlating physical damage with functional failure in targets, Cao [7] combined Fault Tree Analysis with damage simulation to achieve a systematic vulnerability analysis, mapping from physical damage of target components to functional failure of the target system. Based on these, Wu et al. further developed a general assessment framework encompassing target characteristics, damage element analysis, and vulnerability assessment. They also emphasized the importance of establishing detailed and accurate damage criteria. Aiming at the issues of narrow applicability, low efficiency, and empirical formula dependence in existing damage criteria models for target vulnerability, this paper proposes a more comprehensive and standardized calculation method to enhance accuracy.

The fidelity of damage assessment is fundamentally predicated on the precise acquisition of intersection parameters, specifically relative position, impact velocity, and obliquity [8]. Early researchers employed grid-based mathematical models [9] and finite micro-element methods [10] to discretize targets and estimate damage probabilities based on component vulnerability. However, these discretization approaches primarily rely on static mapping, limiting their ability to resolve the instantaneous kinematic vectors required for dynamic evaluation. To enhance physical fidelity, Lomazzi et al. [11] integrated ray-tracing algorithms with ballistic penetration models, significantly improving the accuracy of component failure analysis. Nevertheless, the inherent complexity of ray traversal imposes a prohibitive computational burden, rendering it inefficient for time-sensitive applications. While recent advancements have introduced spatiotemporal layering models to manage intersection uncertainty [12] or analytical methods for real-time velocity estimation [13], a critical bottleneck

remains in APS scenarios. However, in active interception scenarios, the large number of damage elements generated by the interceptor's fragmenting warhead prevents existing methods from ensuring rapid calculation of intersection results. This hinders the APS from obtaining timely evaluation feedback, thereby affecting interception efficiency.

The quantification of damage probability serves not merely as the definitive metric for evaluating terminal lethality but as the pivotal objective function for optimizing the operational efficacy of the APS. To capture the stochastic nature of such encounters, Liu [14] employed Monte Carlo simulations to derive statistical expectations of interception success. Building on this, Li [15] conducted sensitivity analyses to elucidate the coupling effects between systemic errors and the geometric intersection of protective munitions, while Yu et al. [16] developed specialized algorithms to accelerate the vulnerability analysis of missile compartments. Furthermore, Liu et al. [17] experimentally validated the correlation between interception conditions (e.g.,, intersection angles) and damage probability, demonstrating the critical role of parameter tuning in enhancing interception efficiency. However, current methodologies typically decouple the terminal damage mechanism from the dynamic projectile-target intersection process, failing to establish the functional feedback required to inversely optimize the initial firing parameters based on maximizing lethal efficacy. Consequently, existing models are insufficient to support the integrated design of guidance and warhead parameters essential for ensuring interception efficiency under uncertainty.

In this study, a representative rocket model is constructed based on the characteristics of mainstream individual anti-tank rockets. Target characteristic analysis is performed to identify key components and partition the projectile into distinct damage zones. Subsequently, multi-zone damage criteria are established through a combination of theoretical analysis and numerical simulations. Finally, a full-process damage assessment methodology is realized by integrating these criteria with a high-efficiency algorithm for calculating projectile-target intersection. In Section 2, a target characteristic analysis is conducted, identifying key components in the damage phase using the damage tree method, and defining damage zones to establish the correlation between fragment impact locations and damage modes. In Section 3, equivalent models for each zone are established, component failure conditions are theoretically analyzed, and predictive models for the damage criteria of each zone are established based on numerical simulations. In Section 4, a mathematical model for predicting the intersection parameters between fragments and the rocket is established using the "point-to-surface intersection method." Based on this, a damage probability prediction model is constructed using the Monte Carlo method to simulate the stochasticity of the rocket and interceptor intersection location. In Section 5, the influence of

intersection and interception parameters on damage probability is systematically analyzed. The damage assessment methodology and system established in this study significantly improve evaluation accuracy and efficiency, offering a scientific basis for APS intercept parameter design.

2. Rocket target characteristics analysis

A systematic analysis of the target characteristics of a typical rocket is conducted in this section to explore potential damage modes under interception. First, the rocket's operating principle, structures, and functions are analyzed. Second, key components in the damage phase are identified using the damage tree method. Finally, possible damage modes are analyzed by combining the functional characteristics of these key components, and a correlation between fragment impact location and damage mode is established by partitioning the damage zones.

2.1 Structure and function

The core function of the anti-tank rocket is to damage armored targets. The process from launch to impact is generally divided into three stages: the launch phase, the acceleration phase, and the terminal damage phase. In the launch phase, the rocket acquires its initial velocity from the propellant inside the launch tube. In the acceleration phase, the rocket's engine ignites to achieve secondary acceleration. In the terminal damage phase, the rocket impacts the target, the piezoelectric fuse triggers, and the warhead generates a shaped charge jet to damage the armor.

The internal structure of a typical rocket is shown in Fig. 1 [18,19]. The rocket's propulsion system is composed of the nozzles, engine, and igniter, through which continuous thrust is provided primarily during the acceleration phase. The stabilization system is composed of the tail fins and turbine, which are responsible for maintaining the rocket’s flight stability during both the acceleration and terminal damage phases. Furthermore, the warhead system is composed of the fuse, ballistic cap, conductive cone, liner, and charge to ensure effective damage to the target during the terminal damage phase. As the rocket has completed acceleration when interception occurs, the analysis is focused on the terminal damage phase. The specific functions, materials, and types of components involved in this phase are further analyzed and presented in Table 1.

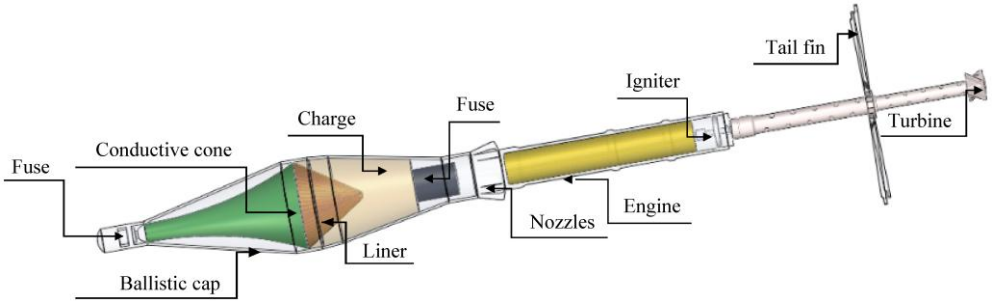

Fig. 1. The internal structure of a typical rocket.

Table 1

Component information of the stabilization system and warhead system of the rocket.

System	Component	Core Function	Material/Model
Stabilization system	Tail fins	Maintain flight stability	Alloy steel
	Turbine	Maintain flight stability	Alloy steel
Warhead system	Fuse	Detonate warhead upon target impact	Piezoelectric fuse
	Ballistic cap	Protect internal warhead structure, connect fuse circuit	Aluminum alloy
	Conductive cone	Connect fuse circuit	Aluminum alloy
	Liner	Generate metallic jet	Copper
	Charge	Explode to form a detonation wave to collapse the liner	RDX-based high energy mixed explosive

2.2 Damage tree and key components of the rocket

The rocket is composed of multiple components, with its terminal damage capability being markedly degraded upon the damage of certain critical parts. These components are defined as key components. To systematically identify critical components, the damage levels of the rocket are first categorized into the following two levels based on the extent of capability impairment: Level I (stability function damage) and Level II (terminal effectiveness damage). Second, as key components differ for each damage level, the damage tree analysis method was used to identify the key components for each level. The method delineates the propagation path from component failure to system impairment via logical associations. Damage trees corresponding to the damage levels were established by combining the core functions of the components in Table 1, as shown in Fig. 2.

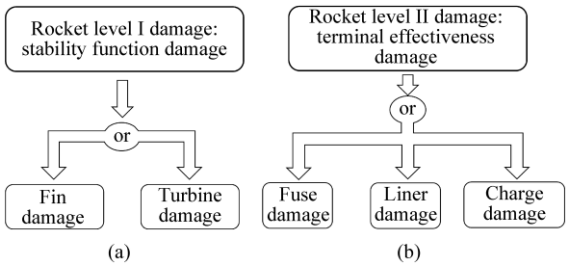

Fig. 2. Damage trees for the rocket. (a) Rocket Level I damage; (b) Rocket Level II damage.

Under engagement, damage to the stabilization system can cause the rocket's trajectory to deviate, reducing the probability of hitting the target. On the other hand, damage to the fuse, liner, or charge will directly lead to premature detonation or the inability to form an effective jet, resulting in a substantial loss of terminal damage

effectiveness [20]. Given that damaging the armored target is the final assessment criterion, the key components of the rocket are determined to be fuse, liner, and charge.

2.3 Partitioning of damage zones

Given that key components are distributed across different zones of the rocket's body and the final damage mode is primarily defined by the failure of specific components, further analysis of the key components' functions, materials, and structures is conducted. A component failure-damage mode correlation tree is established, and damage zones are defined based on the damage modes.

The fuse head is located at the top of the rocket, and its internal structure is shown in Fig. 3. When the piezoelectric block is subjected to sufficient impact pressure, the piezoelectric crystals behind it generate a current due to the positive piezoelectric effect. This current is output through the fuse head and forms a closed circuit through the rocket's body, activating the electric detonator at the base of the fuse to detonate the explosive charge, as shown in Fig. 4. Therefore, fuse damage can result in two scenarios: if the axial pressure F on the piezoelectric crystal exceeds the critical pressure, the fuse triggers, causing the rocket to explode before reaching the target. The damage mode in this case is "Premature Detonation". If a fragment hits the side of the fuse head and damages the internal circuitry, the fuse system will completely lose its detonation function. The rocket will then fail to detonate the explosive charge even upon target impact, resulting in a "misfire" damage mode.

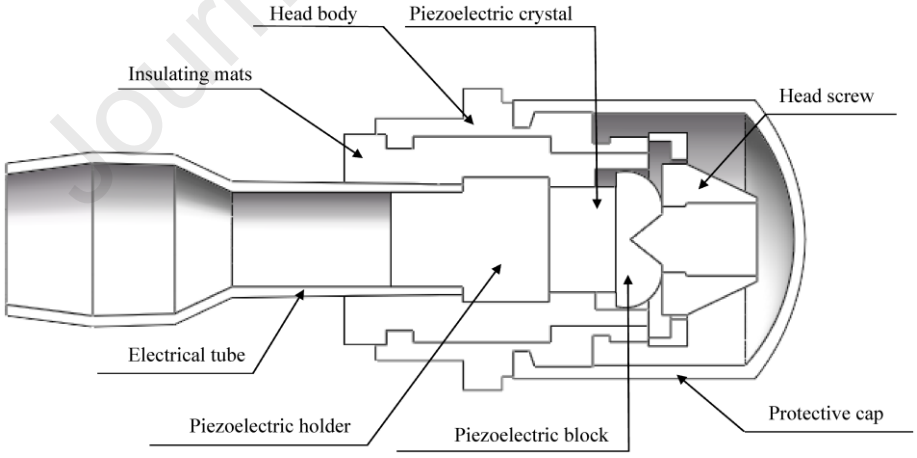

Fig. 3. Internal structure composition of the fuse head.

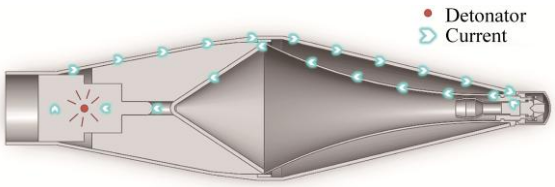

Fig. 4. Activation of the electric detonator by current generated in the fuse head.

The liner is located at the front of the warhead and is made of copper. Existing research indicates that the

integrity of the liner is a key factor influencing the penetration capability of the shaped charge jet. When a fragment penetrates the rocket body and hits the liner, the penetration power of the shaped charge jet decreases by more than 70%. When two or more fragments penetrate the rocket body and hit the liner, the power of the warhead decreases by more than 90% [21]. Therefore, when the liner is hit by two or more fragments, the rocket's damage mode is "loss of warhead power".

The charge in the rocket warhead is a high energy mixed explosive with RDX as the main component. When a fragment hits the charge within a certain speed and angle range, the explosive charge will detonate prematurely. The rocket's damage mode in this case is "premature detonation".

Based on the damage modes corresponding to the failure of different key components, a component failure-damage mode correlation tree is established, as shown in Fig. 5, which serves as the basis for partitioning the rocket into specific damage zones, as shown in Fig. 6. The specific damage zones and their corresponding damage modes are classified as follows:

(1) The fragment hitting the top of the fuse head (A_1) zone causes premature detonation. The fragment striking the side of the fuse head (A_2) zone causes "misfire".

(2) Two or more fragments penetrating the ballistic cap and conductive cone to damage the liner (*B*) zone causes "loss of warhead power".

(3) The fragment impacting the charge (*C*) zone causes "premature detonation".

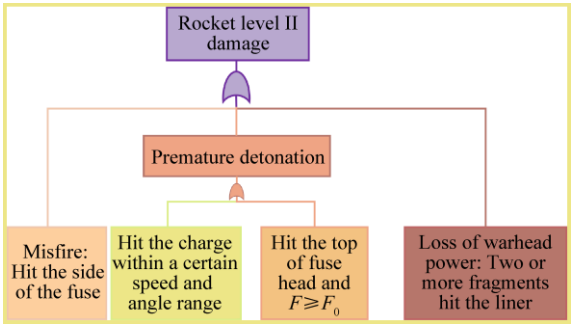

Fig. 5. Component failure-damage mode correlation tree.

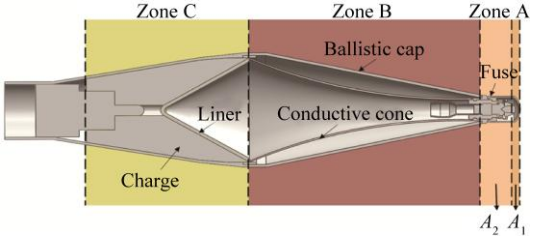

Fig. 6. Rocket damage zone division.

3Damage criteria prediction models

To calculate the damage criteria for the rocket, an equivalent model is established for each damage zone, and the failure conditions for components are determined through theoretical analysis. Then, simulations were performed using the LS-DYNA Hydrocode, based on the failure condition, to calculate and determine the critical fragment velocities that lead to each damage mode. Finally, damage criteria prediction models for each region were established by combining the theoretical analysis and numerical simulation results.

3.1 Fuse zone

Upon the impact of the piezoelectric fuse, the impact force acts on the piezoelectric crystal, causing it to generate electric charges via the positive piezoelectric effect. These charges are subsequently transmitted through the projectile's internal circuitry to the base of the fuse. To quantitatively characterize this process, an equivalent circuit is established (Fig. 7.): the piezoelectric crystal is represented as a charge source Q in parallel with capacitance; the distributed capacitance of the projectile body is incorporated into the total capacitance; and the base of the fuse is represented as a parallel unit consisting of an equivalent resistor and capacitor. Based on Kirchhoff's current law, the governing differential equation of the system is formulated as follows:

$$\frac{U}{R}+C\frac{\mathrm{d}U}{\mathrm{d}t}=\frac{\mathrm{d}Q}{\mathrm{d}t} \tag{1}$$

$$\frac{dU}{dt}+\frac{1}{CR}U=\frac{1}{C}\frac{dQ}{dt} \tag{2}$$

where R is the equivalent resistance of the electric detonator (Ω); C is the total equivalent capacitance of the system (F), including the capacitance of the crystal and the distributed capacitance of the projectile; Q is the charge generated by the piezoelectric crystal upon impact (A); U is the transient voltage across the piezoelectric crystal and the fuse base (V).

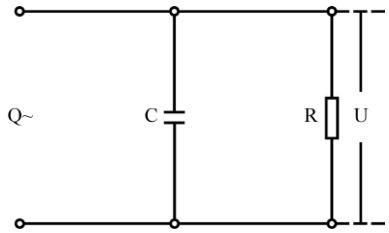

Fig. 7. Fuse equivalent circuit.

Assume that the charge Q is proportional to the axial force F (N) on the piezoelectric crystal. The

relationship between Q and F can be expressed as:

$$Q = d_{33}F \tag{3}$$

where d_{33} is the piezoelectric modulus of the crystal, and F is the axial force exerted on it. With the initial conditions $t = 0$, $U = 0$, the formula can be expressed as:

$$U = \frac{d_{33}}{C}F \tag{4}$$

The total capacitance of the piezoelectric crystal, rocket body, and fuse bottom is 460 pF; the resistance of the detonator R is 10^8 Ω and the detonation voltage U is 3000 V [22]. Substituting these values into the formula, the axial pressure required for the piezoelectric crystal is 2560 N. Since the piezoelectric crystal is subjected to an assembly preload (F_J) of 780 N generated by the head screw, the impact force must first counteract this structural pre-stress. Therefore, the total absolute critical pressure required for the crystal to trigger the fuse is calculated as 2560 N + 780 N = 3340 N.

The 1/2 simulation model was established to calculate the critical fragment velocity required to make the piezoelectric crystal reach its critical pressure, as shown in Fig. 8. The fragment was modeled as a tungsten alloy sphere, and the piezoelectric crystal was selected as GTQ-3 lead zirconate titanate. The piezoelectric seat is made of FX505 phenolic resin, and the remaining load-bearing structures are made of 2A12 aluminum alloy. The material constitutive models were set as follows: the piezoelectric seat uses the Plastic-Kinematic elastoplastic model; the piezoelectric crystal uses the Johnson-Holmquist-Ceramics model; the metal structural components use the Johnson-Cook model. The key simulation parameters for each material are shown in Tables 2–4.

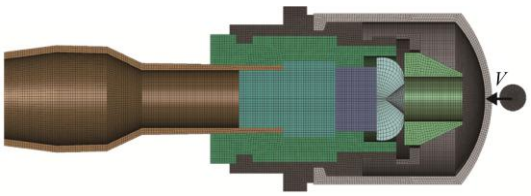

Fig. 8. Simulation model of the fuse area.

Table 2

Johnson – Cook parameters and equation of state parameters for materials [23–25].

Materials	ρ/(g·cm^{-3})	A/MPa	B/MPa	n	c	m	s_1	γ_0	C_0/(m·s^{-1})
Aluminum alloy	2.77	265	426	0.34	0.015	1	1.338	1.97	5328
Tungsten alloy	17.6	1506	177	0.12	0.016	1	1.44	1.58	4029
Copper	8.9	90	292	0.31	0.025	1.09	1.49	2.02	3940

Table 3

Key Parameters for FX505 phenolic resin PLASTIC_KINEMATIC material model [26].

ρ/(g·cm^{-3})	E/GPa	G/GPa	A/MPa	μ	β	Failure strain
1.8	9.0	3.46	265	0.3	0.8	1

Table 4

Key Parameters for GTQ-3 JOHNSON_HOLMQUIST_CERAMICS material model [27].

*Mat-Johnson-Holmquist-Ceramic					
Parameter	values	Parameter	values	Parameter	values
Density ρ/(g·cm^{-3})	3.70	Intact strength parameter N	0.60	Maximum normalized fractured strength *SFMAX*	0.03
Shear modulus G/GPa	90.16	Reference strain rate EPSI	1.0	Hugoniot elastic limit HEL/GPa	6.70
Intact normalized strength A	0.88	Maximum tensile pressure strength T/GPa	0.262	Pressure Component at the Hugoniot elastic limit PHEL/GPa	0.0363
Fractured normalized strength B	0.28	First pressure coefficient	130.95	BETA	1.0
Strength parameter C	0.003	Second pressure coefficient K_2 /GPa	0	Parameter for plastic strain to fracture D_1	0.005
Fractured strength parameter M	0.64	Third pressure coefficient K_3 /GPa	0	Parameter for plastic strain to fracture D_2	0.70
Failure criteria FS	1.60				

Given the small volume of the fuse head, the influence of fragment velocity direction deviation was ignored in this study. Accordingly, the simulation model was simplified to the condition that the fragment always penetrates vertically (the velocity vector aligns with the fuse axis), and the impact point is fixed at the geometric center of the fuse head. The fuse velocity was set to the rocket's terminal velocity of 295 m/s. To quantify the damage criterion, a parameter sweep of the fragment velocity was executed from 1 m/s to 10 m/s with a fine gradient of 1 m/s, totaling 10 simulation runs. This specific gradient was chosen because it provides sufficient resolution to capture the triggering threshold of the piezoelectric crystal without incurring redundant computational costs. The accuracy of the results relies on a theoretical model (equivalent circuit) coupled with the calibrated material model.

The keyword *Database-Rcforc was used to output the contact force on the piezoelectric crystal. The analysis of the simulation results showed that the fragment velocity required to reach the critical pressure of the crystal is between 3 m/s and 4 m/s. The axial force time history curves for these two velocities are shown in Fig. 9. At fragment speeds of 3 m/s and 4 m/s, the axial forces on the piezoelectric crystal reached 3291 N and 3773 N, respectively. Therefore, the critical speed threshold for the fragment to trigger the piezoelectric effect is 4 m/s.

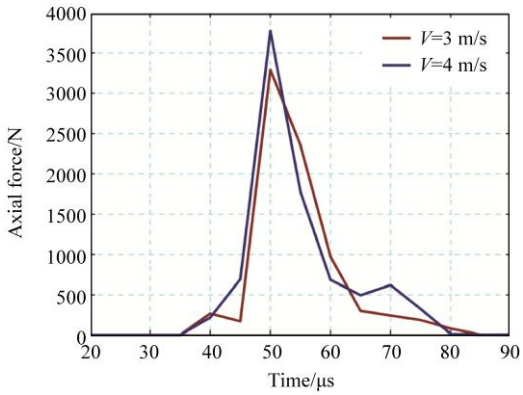

Fig. 9. The axial force time history curves.

Based on the function analysis and the critical force threshold, the damage modes for the fuse zone are strictly defined by the fragment's impact trajectory and velocity. Specifically, if a fragment hits the side of the fuse head, it destroys the fuse system, resulting in a "Misfire." Conversely, if the fragment hits the top of the fuse head and generates an axial force on the piezoelectric crystal exceeding the critical threshold ($F \geq 3340N$, which corresponds to an impact velocity of $V \geq 4\text{m/s}$), it successfully triggers a "Premature Detonation."

3.2Liner zone

When the rocket is intercepted, its liner is protected by the rocket ogive and the tapered hood. The fragment must penetrate these two layers sequentially before hitting the liner. An equivalent model is established as shown in Fig. 10(a). When fragments hit the tapered hood, its velocity direction and magnitude determine whether it hits the liner. To represent the fragment's velocity direction, the coordinate system is established with the impact point of the fragment as the origin *O*. The *XY* plane is aligned with the symmetry plane of the rocket body, where the *X*-axis is along the tangent direction of the ogive, and the *Y*-axis is along the normal direction of the ogive, as shown in Fig. 10(a). In this coordinate system, the velocity V is orthogonally decomposed into the component V_z along the *Z*-axis and the component V_{xy} in the *XY*-plane. The angle between V_{xy} and V is defined as the pitch angle θ ; the component V_{xy} is further decomposed into V_x and V_y along the respective coordinate axes, and the angle between V_x and V_{xy} is defined as the azimuth angle φ , as shown in Fig. 10(b). Since the projectile body is a rotationally symmetric structure, the damage criterion for any intersection point can be equivalently represented by the functional relationship involving the pitch angle θ , azimuth angle φ , and velocity V.

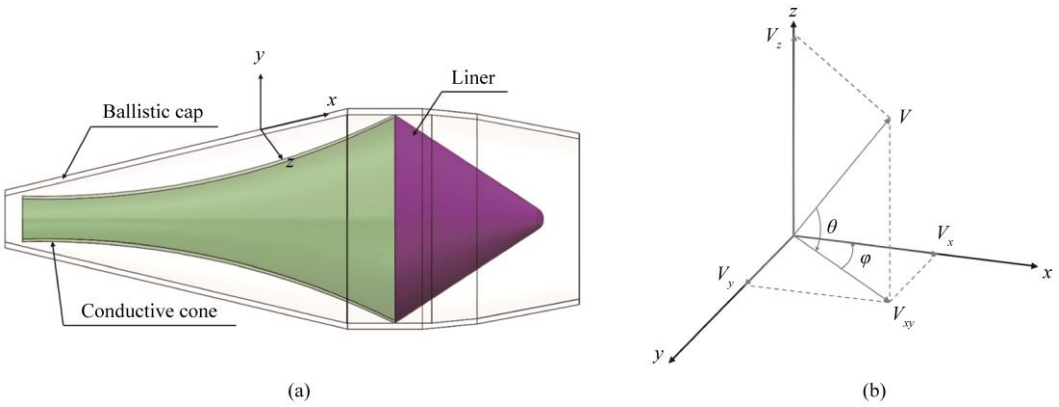

Fig. 10. Equivalent model of the liner zone and fragment coordinate system. (a) Equivalent model and the damage element coordinate system established at a point on the ballistic cap; (b) Vector decomposition of velocity *V*.

Geometric analysis is performed on the equivalent model of the liner zone. The necessary condition for the liner to be struck by a fragment is that the fragment trajectory must pass through the liner's base circle. Consequently, by analyzing the trajectory, equations governing the azimuth and pitch angles required for a successful hit are established. Since the conductive cone is thin, the fragment's velocity direction is assumed to remain invariant during its motion. The projected trajectories in the *XY* planes when the fragment reaches the base circle are illustrated in Fig. 11(a). Relationships are established between the horizontal displacement along the projectile axis and the vertical displacement as follows:

$$\frac{x_1}{r+y_1}=\frac{V_x\,\mathrm{Cos}\,\alpha+V_y\,\mathrm{Sin}\,\alpha}{V_y\,\mathrm{Cos}\,\alpha+V_x\,\mathrm{Sin}\,\alpha}=\frac{V\,\mathrm{Cos}\,\theta\,\mathrm{Cos}\,\varphi+V\,\mathrm{Cos}\,\theta\,\mathrm{Sin}\,\varphi\,\tan\alpha}{V\,\mathrm{Cos}\,\theta\,\mathrm{Sin}\,\varphi+V\,\mathrm{Cos}\,\theta\,\mathrm{Cos}\,\varphi\,\tan\alpha}=\frac{1+\tan\varphi\tan\alpha}{\tan\varphi+\tan\alpha} \tag{5}$$

where, x_1 represents the horizontal displacement along the projectile axis, y_1 denotes the distance between the fragment and the center of the base circle (where $-r < y_1 < r$), r is the liner's base radius, $r + y_1$ is the vertical displacement along the projectile axis, and α is the angle between the *x*-axis and the rocket's axis.

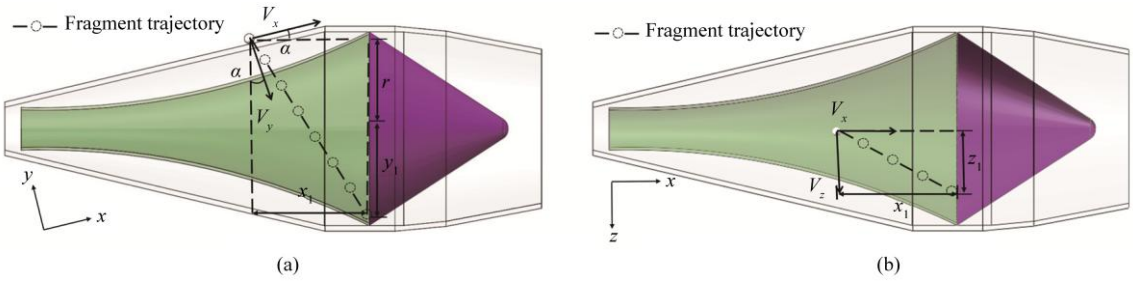

Fig. 11. Geometric Relationship for Parameters. (a) Fragment displacement along the *XY* plane; (b) Fragment displacement along the *XZ* plane.

The projected trajectories in the *XZ* planes when the fragment reaches the base circle are illustrated in Fig. 11(b). Relationships are established between the horizontal displacement along the projectile axis and the vertical displacement as follows:

$$\frac{x_1}{z_1}=\frac{V_x\,\mathrm{Cos}\,\alpha+V_y\,\mathrm{Sin}\,\alpha}{V_z}=\frac{V\,\mathrm{Cos}\,\theta\,\mathrm{Cos}\,\varphi\,\mathrm{Cos}\,\alpha+V\,\mathrm{Cos}\,\theta\,\mathrm{Sin}\,\varphi\,\mathrm{Sin}\,\alpha}{V\,\mathrm{Sin}\,\theta}=\mathrm{Cot}\theta(\mathrm{Cos}\,\varphi\,\mathrm{Cos}\,\alpha+\mathrm{Sin}\,\varphi\,\mathrm{Sin}\,\alpha) \quad (6)$$

where, x_1 represents the horizontal displacement along the projectile axis, z_1 denotes the distance between the fragment and the center of the base circle.

As the trajectory passes through the base circle, y_1 and z_1 satisfy the relationship $y_1^2+z_1^2\le r^2$. By integrating Eqs. (5) and (6), the relationship between the azimuth and pitch angles is derived:

$$\left(\frac{\tan\varphi+\tan\alpha}{1+\tan\varphi\tan\alpha}-\frac{r}{x_1}\right)^2+\left(\frac{\tan\theta}{\mathrm{Cos}\,\varphi\,\mathrm{Cos}\,\alpha+\mathrm{Sin}\,\varphi\,\mathrm{Sin}\,\alpha}\right)^2\le\left(\frac{r}{x_1}\right)^2 \quad (7)$$

For each point in the liner zone, the corresponding azimuth and pitch angles for the damage element when the warhead liner fails can be obtained by substituting $\alpha, r, x_1, \theta, \varphi$ into the above equations.

When the fragment's azimuth and pitch angles meet the failure condition, sufficient kinetic energy is still required to hit the liner. Simulations were performed to determine the velocity magnitude range required for the fragment to hit the liner by analyzing the penetration process of the liner zone at different speeds. In the simulation setup, the fragment was modeled as a 3.5 mm diameter sphere, and the thicknesses of the ballistic cap, conductive cone, and liner were specified as 2 mm, 1 mm, and 2 mm, respectively. The Johnson-Cook model was used to describe the material behavior of the fragment, ballistic cap, conductive cone, and liner, with relevant parameters shown in Table 2. The utilization of these rigorously calibrated and widely validated constitutive parameters ensures computational accuracy of the penetration simulation results. Given the wide range of fragment velocities, pursuing sub-100 m/s precision would incur massive redundant computational costs without yielding any practical benefits for the macro-level probability assessment. To determine the effective velocity range, a parameter sweep of 23 simulation runs was conducted from 800 m/s to 3000 m/s with a discrete gradient of 100 m/s, and the velocity angle was chosen according to Eq. (7).

Simulation results for different fragment speeds are analyzed, with representative operating conditions selected: fragment speeds of 800 m/s, 1500 m/s, 1800 m/s, and 2200 m/s. The kinetic energy and velocity time history curves of the fragments at various initial velocities are presented in Fig. 12. As shown in the figure, the kinetic energy and velocity curves of the fragment exhibit three successive drops, corresponding to the three

distinct stages: ballistic cap penetration stage, conductive cone penetration stage, and liner penetration stage. At an initial fragment velocity of 800 m/s, the velocity at the start of the third stage is only 176 m/s, which is insufficient to perforate the liner, resulting only in minor deformation. When the initial velocity is 1500 m/s, the kinetic energy and velocity at the start of the third stage are 78 J and 737 m/s, respectively, leading to successful perforation. Similarly, at 1800 m/s, the kinetic energy and velocity are 38 J and 700 m/s, respectively, and the liner is perforated. However, at a velocity of 2200 m/s, the kinetic energy and velocity at the start of the third stage are 30 J and 1300 m/s, and the liner cannot be perforated, showing only slight deformation.

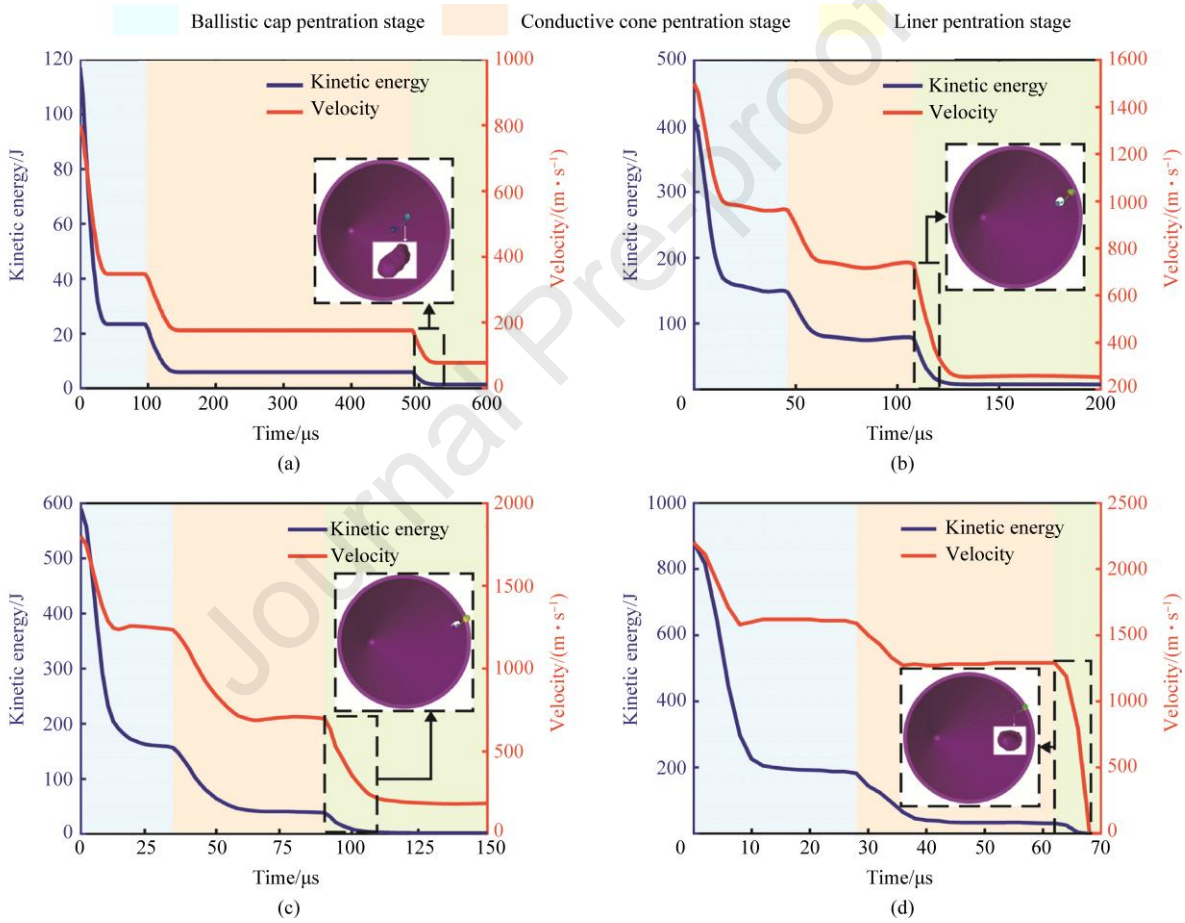

Fig. 12. Kinetic energy and velocity time history curves of fragments at different initial velocities. (a) 800 m/s; (b) 1500 m/s; (c) 1800 m/s; (d) 2200 m/s.

Analysis indicates that at lower initial velocities, kinetic energy is rapidly dissipated during the first two stages, preventing liner perforation in the third stage. Conversely, as the initial velocity increases, mass loss due to erosion during the initial penetration phases becomes more pronounced. Beyond a certain threshold, the residual kinetic energy is insufficient to perforate the liner in the final stage. In summary, the liner cannot be

perforated at either excessively low or excessively high velocities. The effective velocity range is further refined using the "up-and-down method," resulting in an effective velocity range of 1100 m/s to 1800 m/s.

In summary, the damage criterion for the liner zone (Loss of warhead power) is triggered when two or more fragments hit and their kinematic parameters simultaneously satisfy the geometric trajectory constraints defined by Eq. (7) and the effective penetration velocity range of $1100\ \text{m/s} \le V \le 1800\ \text{m/s}$.

3.3 Charge zone

For the charge zone (Zone *C*), the primary damage mode is defined as "Premature Detonation," which is governed by the Shock-to-Detonation Transition. The equivalent model shown in Fig. 13 was established. Due to the geometry of the liner and cap, the critical initiation velocity varies with impact location. Therefore, the charge zone was divided into three zones. The damage criterion for each region, defined by the fragment's impact velocity and obliquity, is represented by the criterion at the central point.

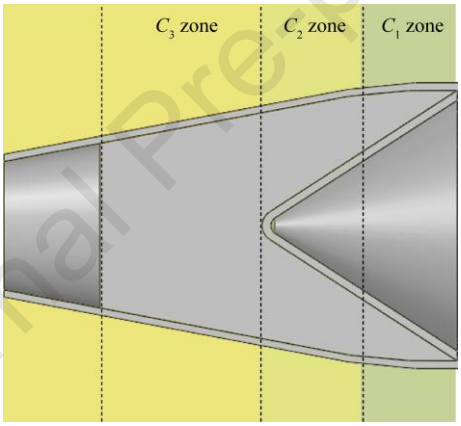

Fig. 13. Equivalent model and division of charge damage zone.

Simulations of the fragment impacts on the explosive at various velocities were performed. The simulation model includes the fragment, charge, liner, ballistic cap, and air. Numerical simulations were conducted using the Simplified Arbitrary Lagrangian–Eulerian (S-ALE) method. Contacts between components described with multi-material arbitrary Lagrangian Eulerian (MMALE) (air, warhead) and Lagrangian (remaining components) element formulations were modeled with the *Constrained_Lagrange_In_Solid fluid-structure interaction algorithm. Discretization of the simulation components, performed using ALTAIR HyperMesh software, is shown in Fig. 14. In the discretization the distance between the neighboring nodes of components of the warhead, the ballistic cap and fragments equaled $\Delta x=\Delta y=\Delta z=1\ \text{mm}$.

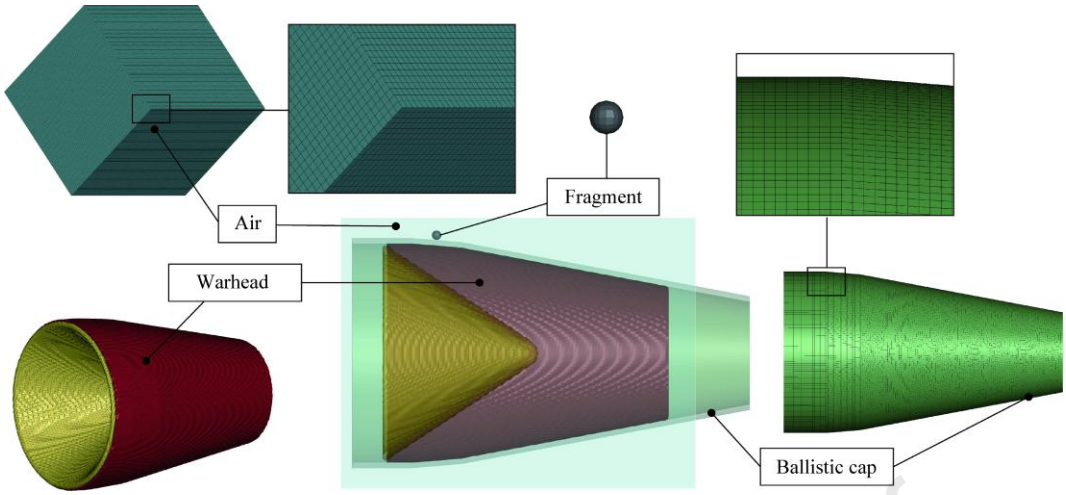

Fig. 14. Discretization of the simulation model for the charge zone.

The explosive reaction was represented using the Ignition and Growth (IG) model, and both the unreacted explosive and reaction products were described by the JWL equation of state.

$$P = A\left(1-\frac{\omega}{R_1 V}\right)\mathrm{e}^{-R_1 V} + B\left(1-\frac{\omega}{R_2 V}\right)\mathrm{e}^{-R_2 V} + \frac{\omega E}{V} \tag{8}$$

where P is the pressure, V is the relative volume, T is the temperature, ω is the Gruneisen coefficient, E is the internal energy and A, B, R_1, R_2 are the JWL constants (see Table 5 below).

Table 5

EOS parameters for Comp-B [28].

State	A/Mbar	B/Mbar	R_1	R_2	ω
unreacted	778.1	−0.05031	11.3	1.13	0.667
reacted	5.242	0.07678	4.2	1.1	0.34

The IG models' main feature is the rate equation governing the dynamics of the fraction of unreacted explosive, which is transformed into detonation products (but not necessarily through a detonation process).

$$\frac{\mathrm{d}\lambda}{\mathrm{d}t} = I\left(1-\lambda\right)^b\left(\frac{\rho}{\rho_0}-1-a\right)^x + G_1\left(1-\lambda\right)^c\lambda^d p^y + G_2\left(1-\lambda\right)^e\lambda^g p^z \tag{9}$$

where I, b, a, x, G_1, c, d, y, G_2, e, g, z are calibration constants and the first, second, and third terms on the right side of Eq. (9) are switched on within the intervals [0, λ_{igmax}], [0, λ_{G1max}] and [0, λ_{G1min}], respectively. The IG parameter values we used in our work are listed in Table 6 below.

Table 6

IG reaction rate model parameter [28].

ρ_0	I/(μs^{-1})	b/Mbar	x	a	c	d	y	e	g	z
1.717	44	0.667	7.0	0.0367	0.667	0.333	2.0	0.222	1.0	2.0
G_1 /(Mbar^{-2}·μs^{-1})	λ_{igmax}	λ_{G1max}	λ_{G1min}							
1000	0.022	0.7	0.0							

The accuracy of the model and simulation parameters was validated against existing experimental results fragments shock initiating Composition B [29]. In the experiment, a cylindrical tungsten alloy fragment impacted a cylindrical charge of Composition B explosive with a steel cover plate. The thickness of the cover plate was 4 mm. The experimentally measured impact initiation threshold velocity was 868.6 m/s, while the simulation predicted 915 m/s. The close agreement validates the effectiveness of the numerical model used in this study.

In the simulation design, θ and φ were varied from 0° to 60° with an interval of 10° to calculate the threshold velocity required for fragment impact initiation, totaling 490 simulation cases. This angular domain was selected because the simulation data points acquired within this range are mathematically sufficient to accurately regress the parameters of the damage criterion model, thereby avoiding redundant computational costs at more extreme angles. For each angular combination, the critical initiation velocity was identified by sweeping the fragment velocity with a 100 m/s discrete interval. Taking the impact scenario at Zone C_1 ($\theta = 0°, \varphi = 60°$) as a representative case, the fragment velocity is 1800 m/s, and the numerical of the fragment impact initiation process are presented in Fig. 15. To rigorously verify the occurrence of detonation, Lagrangian gauge points were embedded to monitor the pressure evolution of the explosive. As visually marked in Fig. 15(a), five gauges are embedded along the fragment impact trajectory with an equidistant spacing of 5 mm. Within 0–7 μs, the pressure evolution and peak values of observation gauges 1 and 2 are nearly identical. At 8 μs, the pressure peak of gauges 3 rises sharply and continues to increase in gauges 4 and 5 thereafter. By tracking the propagation of pressure peaks across these points, we can distinguish whether the initial impact generates a decaying shock wave or successfully amplifies into a stable, self-sustaining detonation wave (as indicated by the "Shock" to "Detonation" transition in Fig. 15(b)). This real-time pressure monitoring plays a critical role in the damage assessment process, providing the definitive physical evidence required to confirm the "Premature Detonation" damage mode.

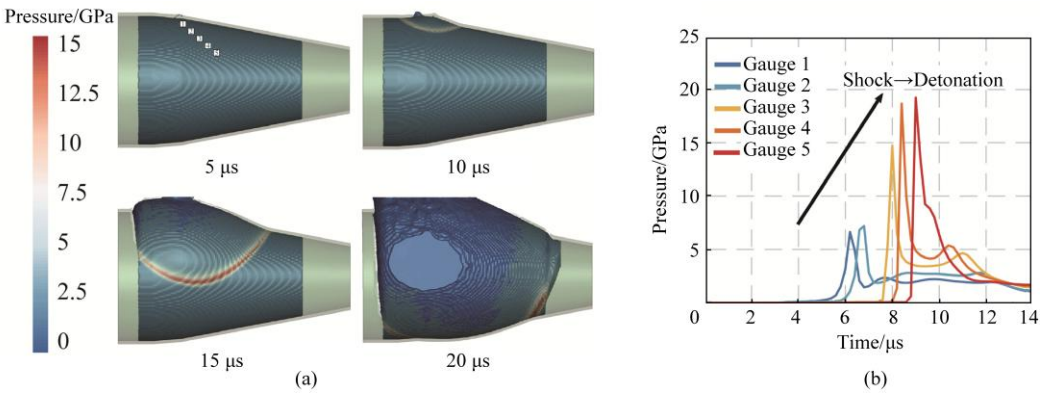

Fig. 15. Numerical of the fragment impact initiation process. (a) Spatiotemporal evolution of the pressure field at characteristic instants; (b) Peak pressure time history curves of five observation gauges.

The simulations yielded the corresponding critical velocities V_{Lin} for different combinations of θ and φ. A function fitting algorithm was applied to the multiple groups of data $(\theta,\ \varphi,\ V_{\mathrm{Lin}})$ to obtain a functional relationship, which serves as the damage criterion for the charge zone. Specifically, the critical initiation velocity V_{Lin} for the three zones (C_1, C_2, C_3) are mathematically expressed as follows:

For Zone C_1:

$$V_{\mathrm{Lin}} \geq (139\mathrm{e}^{-0.64\varphi} + 0.0009\mathrm{e}^{-0.0467\varphi})\theta^4 + 82497\varphi^{-1.4} + 1096.4 \tag{10}$$

For Zone C_2:

$$V_{\mathrm{Lin}} \geq 1.4\varphi^{-2.48} \cdot \theta^4 + 53823\varphi^{-1.35} + 1271.5 \tag{11}$$

For Zone C_3:

$$V_{\mathrm{Lin}} \geq 17.26\varphi^{-3.14} \cdot \theta^4 + 366160\varphi^{-2.03} + 1366.2 \tag{12}$$

The damage mode of "Premature Detonation" is triggered when the fragment velocity V satisfies $V \geq V_{\mathrm{Lin}}$.

This relationship is represented as a fitted surface in a 3D coordinate system (Fig. 16). The fitted surface is mathematically extended to 90° for both θ and φ. This extrapolation is intended to provide a continuous and closed mathematical boundary for the damage criterion model, representing the prediction of thresholds for extreme impacts. From the figure, it is evident that for a fixed θ, the critical impact initiation velocity increases as φ decreases, and the rate of increase becomes progressively steeper. Conversely, for a fixed φ, the critical velocity increases as θ increases, also exhibiting a steeper growth trend. The underlying reasons are as follows: as φ decreases or θ increases, the fragment penetrates the shell and explosive obliquely, enlarging the contact area between the fragment and the explosive while simultaneously increasing the effective thickness of the shell to be penetrated. This causes the critical impact initiation velocity to rise. When φ continues to decrease or θ continues to increase, the contact duration between the fragment and the explosive becomes

shorter, the intensity of the sustained shock wave generated by the impact diminishes, and the mechanical friction–shear interaction is reduced. Consequently, explosive initiation becomes more difficult, and the required critical initiation velocity increases rapidly. In this regime, the dominant factor influencing explosive initiation is the strength of the shock wave produced by the fragment; the shock must be sufficiently intense to trigger detonation, leading to the observed accelerated growth of the critical initiation velocity.

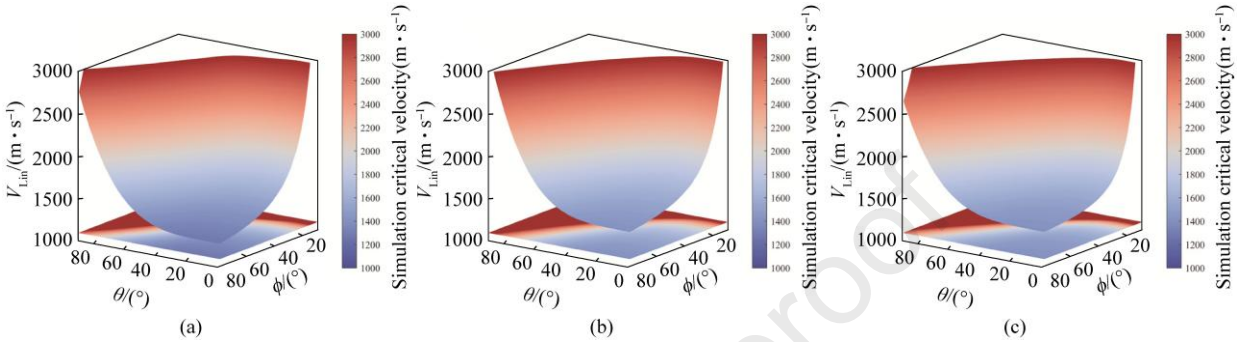

Fig. 16. Fitted surface for damage criteria. (a) C_1 zone; (b) C_2 zone; (c) C_3 zone.

The predictive fidelity of the proposed decoupled parametric model is rigorously evaluated in Fig. 17. The verification analysis is conducted within the 0°–60° simulation design space, comparing the predicted critical velocities (V_{pred}) against the actual numerical simulation results (V_{Lin}). The color gradient maps the pitch angle θ, while the marker shapes categorize the azimuthal angle φ into distinct geometric zones.

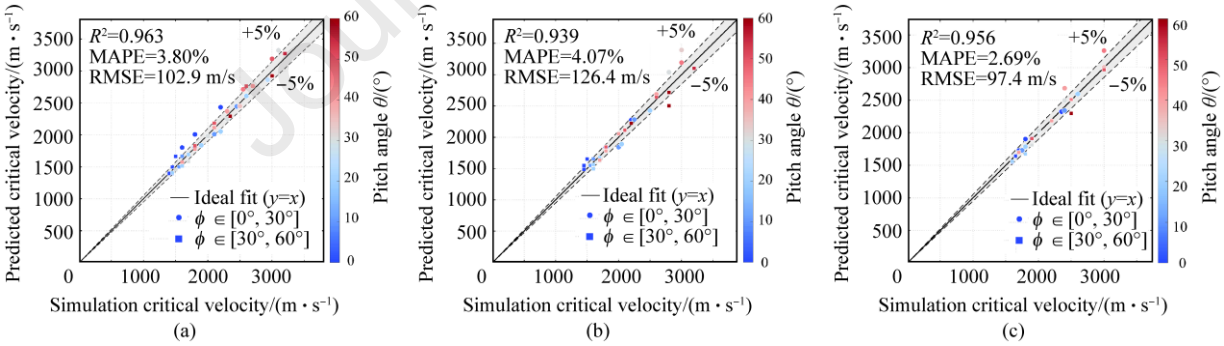

Fig. 17. Comparative parity plots for different charge zones: (a) Zone C_1; (b) Zone C_2; (c) Zone C_3.

Statistically, the model exhibits high-fidelity predictive capabilities across the entire charge zone. Visually, the data points are tightly clustered along the ideal fit line ($y = x$). Notably, the explicitly demarcated 5% relative error band encapsulates nearly all data points. The Coefficient of Determination (R^2) consistently exceeds 0.93 for the entire zone, and the Mean Absolute Percentage Error (MAPE) remains strictly below the 5% threshold. Specifically, Zone C_1 (Fig. 17(a)) shows a balanced and robust performance. Zone C_2 (Fig. 17(b)) exhibits

a marginally higher dispersion in the high-velocity regime. Zone C_3 (Fig. 17(c)) demonstrates the highest precision with an MAPE of only 2.69%.

4Damage assessment method

According to the established damage criteria, the damage mode by fragment can be accurately determined from its intersection parameters. Thus, intersection algorithm between the fragment field and rocket projectile was constructed to compute these parameters. Furthermore, to address the problem of calculating the interceptor's damage probability against the rocket in a practical battlefield context, a full-process assessment model covering the interceptor's launch, flight, intersection, and damage phases was established.

4.1 Flight parameter calculation

The use of appropriate coordinate systems in interception process analysis can greatly simplify computational complexity. However, during data transfer among different calculation stages, multiple coordinate transformations are inevitably involved. Therefore, to facilitate the establishment of subsequent mathematical models and the solution of interception parameters, three coordinate systems are defined as shown in Fig. 18: a fixed coordinate system with the tank gun muzzle O_g as the origin, an interceptor-fixed coordinate system with the interceptor's center O_p as the origin, and a target-fixed coordinate system with the rocket's center O_r as the origin. The matrix transformation method [30] is adopted to achieve translation and transformation between coordinate systems. The coordinate systems involved in the Flight, Fragment Cloud, and encounter calculations and their transformations are illustrated in Fig. 19.

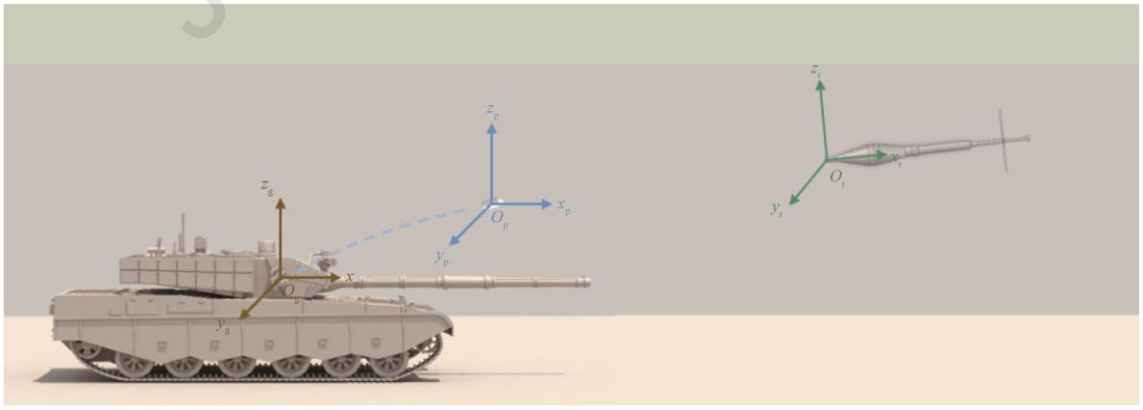

Fig. 18. Spatial distribution of coordinate systems.

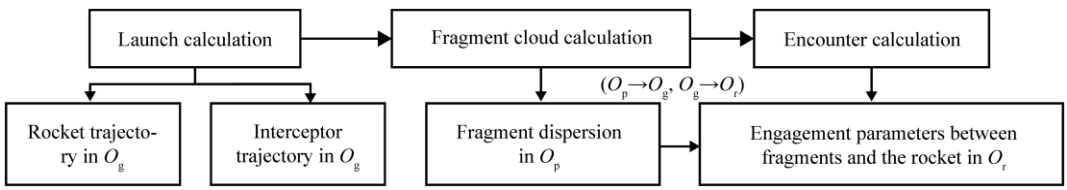

Fig. 19. Coordinate systems throughout the calculation process and associated transformations.

When calculating the flight of the rocket, interceptor, and the fragment cloud dispersion, the influence of aerodynamics on velocity and trajectory must be considered. The aerodynamic drag acting on the target during flight is defined as:

$$F = \frac{1}{2}\rho A C_x v^2 \tag{13}$$

where F is the aerodynamic drag acting on the target; ρ is the air density; A is the windage area of the target; C_x is the aerodynamic drag coefficient; and v is the flight velocity of the target.

During flight, the target undergoes rolling motion, resulting in a variable A and its drag coefficient is also closely related to its shape and flight velocity. However, in practical rocket-interception scenarios, the interceptor and fragments travel over short distances, and only the terminal ballistic phase of the rocket is considered, where the flight distance is likewise short. Therefore, the variations of A and C_x have a negligible effect on the final impact point. Accordingly, A and C_x are assumed constant. The differential equations of motion for the projectile are established as:

$$\begin{cases} \dfrac{\mathrm{d}v_x}{\mathrm{d}t} = -F_x / m \\ \dfrac{\mathrm{d}v_y}{\mathrm{d}t} = -F_y / m \\ \dfrac{\mathrm{d}v_z}{\mathrm{d}t} = -F_z / m - g \end{cases} \tag{14}$$

where, F_x, F_y and F_z denote the components of the total aerodynamic drag force F (given by Eq. (13)) along the x, y and z-axes of their respective coordinate systems; v_x, v_y, and v_z denote the components of the flight velocity along the x, y and z-axes, m represents the mass of the target; and g is the gravitational acceleration. The fourth-order Runge-Kutta method, which is widely employed in engineering numerical analysis, is employed to accurately solve the motion parameters constrained by Eq. (14).

4.2 Encounter parameter calculation

During the rocket-interceptor engagement, only a portion of the fragments can actually strike the rocket. However, intersection calculations must be performed individually for each fragment in all computational approaches. Using the traditional Line-of-Flight method is not only computationally intensive but also introduces errors due to its assumption of strictly linear fragment trajectories [31]. An innovative "Point-to-Surface Distance Method with an Enclosing Shell" was developed in this study to obtain intersection information rapidly and

accurately. First, a cylindrical enclosing shell (Fig. 20) is established around the rocket's effective damage zone. The shell length a is extended by 10 mm at both the front and rear ends of the effective region, and the radius r_1 is increased by 10 mm. The rationale for determining this specific extension distance is intrinsically coupled with the dynamic time-step settings, which will be detailed later in this section. Next, when a fragment is outside the enclosing shell, a coarse time step is used to maximize computational efficiency. Finally, once the fragment enters the shell, a fine time step is adopted to ensure intersection accuracy. Using this method, the times at which a fragment enters the shell and impacts the rocket body are determined sequentially, and the corresponding fragment positions are recorded.

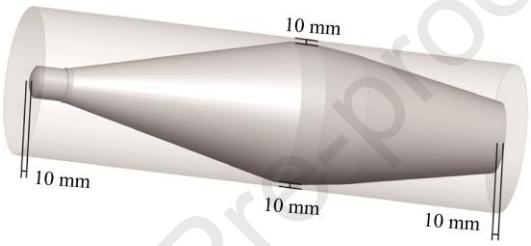

Fig. 20. The cylindrical enclosing shell based on rocket's effective damage zone.

Specifically, when the fragment has not yet entered the enclosing shell, its position in the target coordinate system is denoted as $P_1(x_{r1}, y_{r1}, z_{r1})$. The coarse time step Δt_1 is applied such that $\Delta t_1 \cdot v_p < 5\ \text{mm}$ (where v_p denotes the fragment's maximum velocity), ensuring that no intersection occurs between the fragment and the rocket upon entry into the enclosing shell. In the target-fixed coordinate system, when $y_{r1}^2 + z_{r1}^2 \le r_1^2$ and $-10 \le x_{r1} \le a + 10$, the fragment is determined to be entered the enclosing shell. Once the fragment enters the shell, the fine time step is adopted, and its position is expressed as $P_2(x_{r2}, y_{r2}, z_{r2})$. The fine time step is set to Δt_2 such that $\Delta t_2 \cdot v_p < 1\ \text{mm}$, ensuring that the fragment does not "overshoot" the rocket surface.

As introduced earlier, the cylindrical enclosing shell features a specific 10 mm extension in both the radial and longitudinal directions. The rationale for this dimension is intrinsically coupled with the aforementioned dynamic time-step mechanism. According to the predefined coarse time step (Δt_1) and the maximum fragment velocity (v_p), the maximum displacement of a fragment within a single coarse step is strictly calculated to be less than 5 mm. To completely eliminate a numerical error, where a high-velocity fragment might skip the shell boundary entirely between two consecutive coarse time steps, the extension must be sufficiently larger than this

maximum displacement. Therefore, the 10 mm gap was strategically selected. This specific value provides a safety factor of at least 2.0, ensuring that any incoming fragment will be captured within the extension. This guaranteed capture reliably triggers the transition to the fine time step (Δt_2) for precision intersection calculation.

Since the effective damage region of the rocket is a body of revolution, the rocket's outer surface is represented by a set of parameterized surface equations. Let S_n denote a specific surface of the rocket, which can be described by Eq. (12):

$$S_n=(x_{rsn},y_{rsn},z_{rsn}),\ x_{rsn}\in D_{xn},\ y_{rsn}\in D_{yn},z_{rsn}\in D_{zn} \tag{15}$$

where D_{xn},D_{yn},D_{zn} is the parameter domain of surface. The representative rocket can be represented by six surface equations, as illustrated in Fig. 21(a). For each time step after a fragment penetrates the outer casing, Fig. 21(b) illustrates the relative positions between the fragments and the rocket. The following geometric checks are performed: first, identify which surface equation (i.e.,, in which D_{xn} interval) the fragment's x_{rsn} belongs to; second, compare the distance d_2 from the corresponding z_{rsn}-location of that plane to the *x*-axis with the distance d_1 from the fragment to the *x*-axis; finally, an intersection occurs between the fragment and the rocket when $d_1<d_2$. The expressions for d_1 and d_2 are as follows:

$$d_1=\sqrt{\left(x_{r2}^2+y_{r2}^2\right)},\ d_2=\sqrt{\left(x_{rsn}^2+y_{rsn}^2\right)} \tag{16}$$

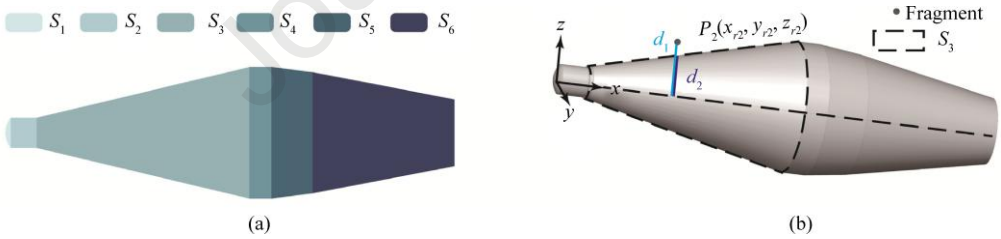

Fig. 21. Schematic of rocket geometric representation and fragment encounter determination.

Unlike conventional cubic bounding boxes which inherently introduce void spaces at their corners, the tightly fitted cylindrical bounding shell is an innovative preliminary filter. Mathematically, for an axisymmetric rocket, the cylinder eliminates the redundant corner volume compared to the cubic bounding boxes. In highly dense fragment cloud interceptions, this volumetric optimization ensures that fragments traversing these empty corners are instantly rejected during the filtering, fundamentally preventing them from erroneously triggering the computationally expensive traversal. The quantitative advantage of this cylindrical bounding shell, particularly in reducing the computational overhead during large-scale stochastic simulations, will be further

substantiated through comparative performance tests in Section 4.3.

4.3 Damage probability

The computational workflow of the damage assessment method is shown in Fig. 22. The flight parameters of the interceptor, the rocket, and fragments are calculated sequentially in respective coordinate systems based on the initial parameters. Fragment–rocket intersection information is obtained using the "Point-to-Surface Distance Method with an Enclosing Shell". By combining the intersection information with the established damage criteria, the damage outcome for the rocket is then determined. The rocket damage outcome is evaluated according to the following priority of damage modes: Premature Detonation > misfire > loss of warhead power.

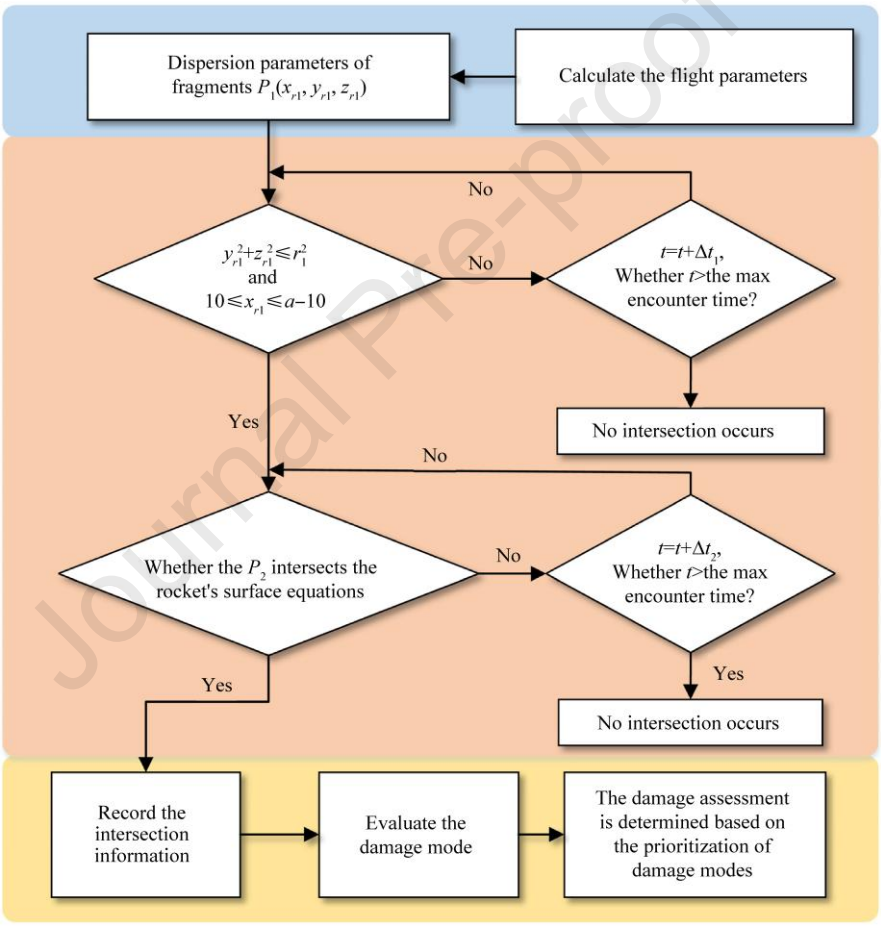

Fig. 22. The computational workflow for determining the damage result.

For a representative scenario, initial parameters (in a fixed coordinate system) are listed in Table 7. The interceptor detonation time is defined as the time at which a stabilized fragment cloud is generated. The foundational parameters for this stabilized fragment cloud are systematically detailed in Table 8. The computed trajectories are displayed in a fixed coordinate system (see Fig. 23). Since the interceptor detonation distance is predefined, the interceptor warhead is triggered at a separation from the rocket. Consequently, the two

trajectories do not intersect. After interceptor warhead detonation, the fragment cloud continues to disperse from the terminal point of the interceptor trajectory. The fragment–rocket intersection result is shown in Fig. 24.

Table 7

Initial parameters for a representative scenario.

Interceptor speed/(m·s^{-1})	Position of the interceptor/m	Detonation time of the interceptor/s	Position of the rocket/m	Velocity of the rocket/(m·s^{-1})
(100,0,0)	（0,0,0）	1	（200,2,2）	(−100,0,0)

Table 8

Foundational parameters of the fragment cloud.

Material	Fragment shape	Fragment mass	Total quantity	velocity	dispersion angle
Tungsten alloy	Sphere	0.4 g	513	2012–2921 m/s	31°

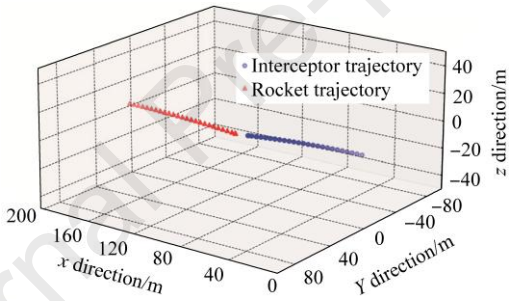

Fig. 23. Interceptor and rocket trajectories.

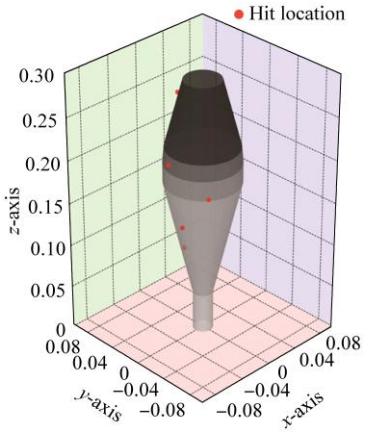

Fig. 24. Fragment–rocket intersection results.

During flight, the rocket is affected by a series of random disturbance factors, resulting in a probabilistic distribution of impact points even under identical launch conditions. Therefore, damage probability is adopted to evaluate the final damage outcome. To realistically assess the lethality of the interceptor warhead detonating at a certain distance from the rocket, a damage probability prediction model is established based on the Monte

Carlo method with Circular Error Probability (CEP) to simulate the stochastic nature of the intersection positions between the rocket and interceptor. Let O_1 denote the expected impact point of the rocket at the instant of interceptor detonation. According to the central limit theorem in probability theory, the perturbations introduced by random factors cause the deviations of the actual impact point from O_1 to follow a normal distribution. With O_1 defined at the origin of the target coordinate system, the probability density function of the actual impact point scattered on the circle centered at O_1 is expressed by Eq. (14).

$$f(y,z)=\frac{1}{2\pi\sigma^{y}\sigma^{z}}\exp\left\{-\frac{1}{2}\left[\frac{(y-\mu_y)^2}{\sigma_y^2}+\frac{(z-\mu_z)^2}{\sigma_z^2}\right]\right\} \tag{17}$$

where, μ_x, μ_z and σ_y^2, σ_z^2 denote the mean and variance of the actual impact point in the O_1Y and O_1Z directions, respectively. It is assumed that $\sigma_y=\sigma_z$ and $\mu_y=\mu_z=0$. The probability that the rocket impacts within the circular region centered at O_1 with radius R is given by Eq. (15).

$$P=P\{(y,z)\in R\}=\iint_{\Omega} f(y,z)\mathrm{d}y\mathrm{d}z=1-\exp(-\frac{R^2}{2\sigma^2}) \tag{18}$$

$$CEP=\sigma\sqrt{2\ln 2} \tag{19}$$

CEP of the rocket under various conditions can be obtained from Eq. (16). Using the Monte Carlo method, M random initial impact positions are generated; for each sampled initial rocket position the damage outcome is computed. By counting the number of trials in which the rocket is classified as damaged and dividing by the total number of trials *M*, the damage probability of the rocket is estimated.

Furthermore, the computational efficiency of the intersection algorithm directly dictates the feasibility of the large-scale Monte Carlo sweeps. To quantitatively substantiate the advantage of the proposed cylindrical bounding shell over the cubic oriented bounding box, a comparative benchmark was conducted. It should be noted that all simulations for the performance benchmarks were executed on a laptop computer equipped with a 12th Gen Intel(R) Core(TM) i7-12700H processor (2.30 GHz) and 16.0 GB of RAM. As shown in Table 9, taking the typical interception scenario in this section as a baseline, by effectively eliminating the mesh traversals caused by the corner void spaces of a cubic box, the cylindrical shell reduces the total time for 1000 iterations by 28.7%.

Table 9

Performance comparison of different bounding methods.

Bounding Method	Number of Monte Carlo simulations	Total Time/s	Improvement

cubic bounding boxes	1000	334	—
cylindrical enclosing shell	1000	238	28.7%

It should be noted, however, that this optimization is primarily tailored for the axisymmetric fuselage of the rocket. While the cylindrical shell lacks the geometric flexibility to efficiently bound non-axisymmetric protrusions such as tail fins, its high efficiency in covering the critical functional zones (fuse, liner and charge) makes it a highly specialized tool for interception assessment.

5 Influence mechanisms of factors on damage probability

During the engagement of the APS, the initial parameters directly affect the final damage probability. To enable efficient interception of incoming rockets, this study analyzes the influence patterns of parameters on the damage probability, and subsequently optimizes the interceptor's parameters to inform interception strategy and interceptor design. As shown in Fig. 25, the angle between the rocket axis and the interceptor axis at the instant of interceptor detonation is defined as the attack angle β; the distance between the interceptor nose and the rocket nose at the moment of detonation is defined as the intercept distance H.

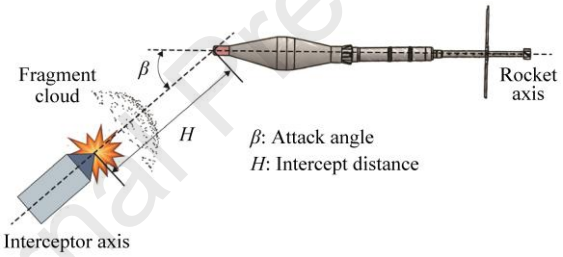

Fig. 25. Geometric definition of interception parameters (β and H) during engagement.

5.1 Coupling analysis of interception parameters

To systematically assess the engagement effectiveness, the influence of two critical parameters—intercept distance (H) and attack angle (β)—on the damage probability was investigated. Considering the kinematic constraints of projectile-target engagement in realistic battlefield scenarios, large crossing angles (e.g., $\beta > 60°$) typically exceed the maneuvering capabilities of the interceptor. Therefore, the attack angle range is constrained to 0°–60°, and the intercept distance is analyzed within the range of 1–6 m. The target and fragment cloud parameters for the Monte Carlo simulations are consistent with the models established in Sections 2 and 3. Specifically, the target is modeled as a typical rocket equipped with a 2A12 aluminum alloy shell (thickness of 2 mm), while the parameters for the fragment cloud are systematically detailed in Table 8. The Monte Carlo simulation was conducted with 1000 runs, yielding a CEP of 0.1 m. The initial velocities were set at 100 m/s for the interceptor and 294 m/s for the rocket. The interceptor's velocity vector aligned with its attack angle, while the rocket traveled along the x-axis of the fixed coordinate system. A fragment cloud of 513 pieces was

configured, consistent with the interceptor warhead studied by our research group. The specific fragment cloud quantity derived from a realistic cylindrical fragmentation warhead design utilized in typical interceptors. Following the classical warhead design principles [32], the total number of fragments is strictly governed by the geometric constraints of the interceptor's casing and the spatial packing arrangement of the predefined tungsten spheres. Given the dimensional baseline of the interceptor model employed in this study, the maximum optimized payload capacity yields exactly 513 fragments.

To justify the selection of 1000 Monte Carlo simulation times, a convergence verification analysis was conducted. Taking a representative interception scenario as the baseline ($H = 1\,\mathrm{m}$, $\beta = 45°$), the damage probability was evaluated across an increasing number of simulations. The probability calculated at the maximum simulation scale ($N = 2000$) was adopted as the benchmark reference. As illustrated in Fig. 26, during the initial phase ($N < 800$), the calculated probability exhibits minor statistical fluctuations, with the maximum relative error peaking at approximately 4%. However, as N approaches and reaches 1000, the probability curve stabilizes remarkably, and the relative error drops to a negligible level, permanently residing well below the 5% tolerance threshold. Therefore, setting the simulation times to 1000 ensures extremely high statistical reliability while maintaining optimal computational efficiency, successfully avoiding redundant calculation costs.

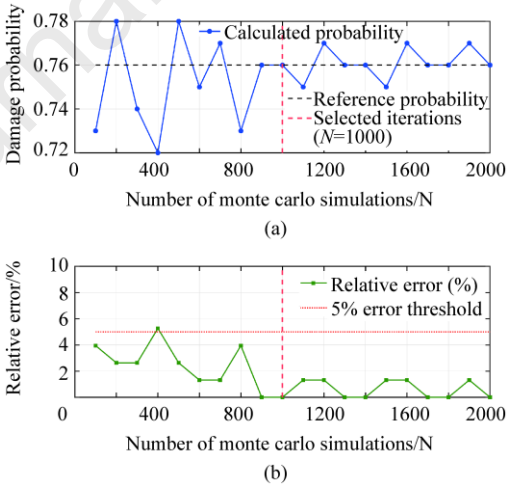

Fig. 26. Convergence verification of the monte carlo simulation. (a) Convergence of damage probability; (b) Decay of relative error.

The coupling effect of intercept distance (H) and attack angle (β) on the damage probability was visualized using a 2D contour heatmap (Fig. 27). A high damage probability Zone ($P > 90\%$) is clearly observed in the near-field ($H \leq 1.0\mathrm{m}$), where the contours are nearly vertical, indicating that near-field interception is highly robust and largely independent of the attack angle.

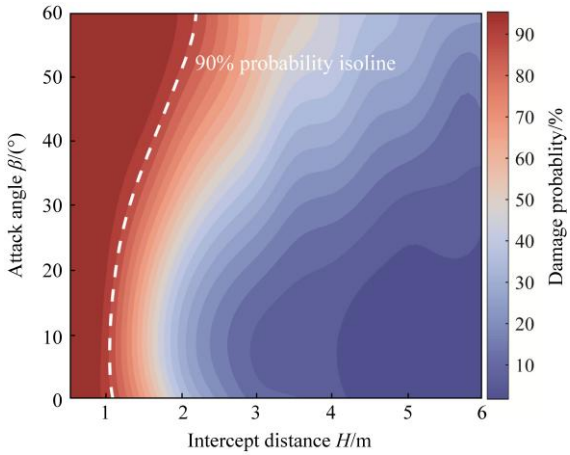

Fig. 27. The coupling effect of intercept distance (*H*) and attack angle (β) on the damage probability.

However, as the distance increases, the boundary of the high-probability zone exhibits a significant non-linear expansion towards larger angles. The 90% probability isoline provides critical quantitative evidence: at a head-on angle ($\beta = 0°$), the boundary is constrained to approximately 1.1 m; in contrast, as the angle increases to $\beta = 60°$, this boundary extends to nearly 2.2 m, effectively doubling the high-probability interception range. Furthermore, when $H \in [2.5,\ 6.0]\text{m}$, the probability contours slope sharply upward to the right. For instance, at an extended distance of 4 m, the damage probability for $\beta = 0°$ collapses into the deep blue zone, $P = 7.9\%$, whereas the $\beta = 60°$ maintains within the light blue area, $P = 45.2\%$. This indicates that increasing the attack angle enlarges the target's vulnerable area, thereby compensating for the probability attenuation caused by distance.

5.2 Mechanism of intercept distance on damage probability

Fig. 27 shows a significant decrease in interception probability with increasing range. To elucidate the degradation mechanism of interception effectiveness, the evolution of damage mode composition with increasing distance for the optimal angle ($\beta = 60°$) is first analyzed, as shown in Fig. 28(a). When $H \le 2\text{m}$, the "Premature Detonation" mode dominates, accounting for over 90% of the outcomes. As the intercept distance increases, the "non-intercept" rate grows rapidly due to the dispersion of the fragment cloud. Crucially, throughout the entire distance range, the proportion of "Loss of Warhead Power" (Power Loss) and "Misfire" remains negligible. This phenomenon is attributed to the high obliquity; fragments hitting Zone *B* at such steep angles fail to meet the criteria established in Section 3. Consequently, the interception outcome at the optimal angle is essentially binary—either premature detonation or complete miss.

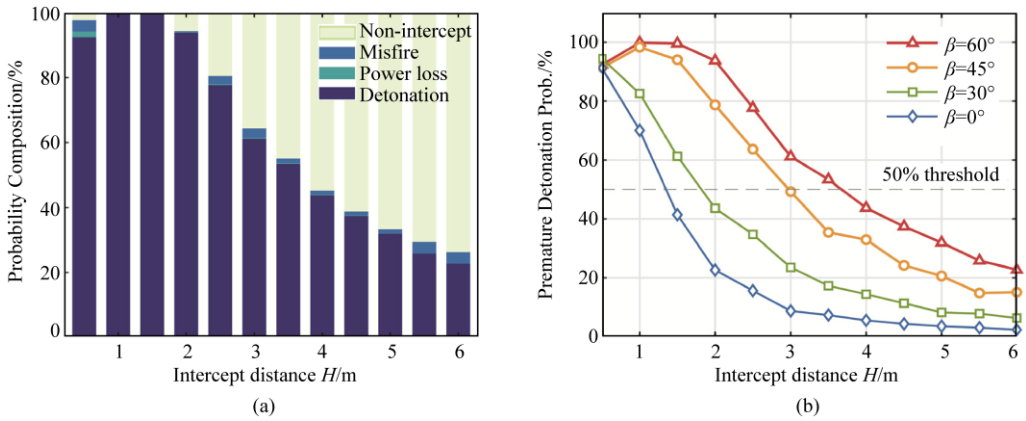

Fig. 28. Mechanism of intercept distance on damage probability. (a) The evolution of damage mode composition for $\beta = 60°$; (b) The attenuation of the "Premature Detonation" mode across different attack angles.

Given that "Premature Detonation" is the primary damage mode, Fig. 28(b) quantifies the attenuation of this mode across different attack angles. The core mechanism driving this universal attenuation is the spatial dispersion of the fragment cloud. Regardless of the attack angle, as the intercept distance increases, the spatial density of the fragments striking the target decreases geometrically due to the initial dispersion angle. This inevitably leads to a sharp decline in the probability of triggering premature detonation. While the distance-driven decay is universal, the rate of attenuation differs significantly between angles; the underlying mechanism driving this angular disparity is further detailed in Section 5.3.

5.3 Mechanism of attack angle on damage probability

As observed in the attenuation curves (Fig. 28(b)), adopting a large attack angle effectively mitigates distance-driven probability decay, extending the 50% success threshold from a mere 1.3 m at $\beta = 0°$ to approximately 3.7 m at $\beta = 60°$. This probabilistic superiority is intrinsically driven by how the attack angle alters the geometric exposure of key components, fundamentally overcoming the target's self-occlusion effect.

Fig. 29(a) elucidates this mechanism by correlating the average number of hits on Zone *B* and Zone *C* with intercept distance using a logarithmic scale to visualize the orders-of-magnitude disparity. At $\beta = 0°$, the Zone *C* is geometrically occluded by the front zones of the rocket. Consequently, fragment hits are concentrated on the Zone *B*, while hit counts on the Zone *C* drop precipitously below 1 at just 1 m. This forces premature detonation to rely solely on the Zone A_1. Conversely, at,the target's side profile exposes directly to the fragment cloud. Even at extended ranges (4–5 m), the Zone *C* hit count remains near 1, providing condition for "Premature Detonation".

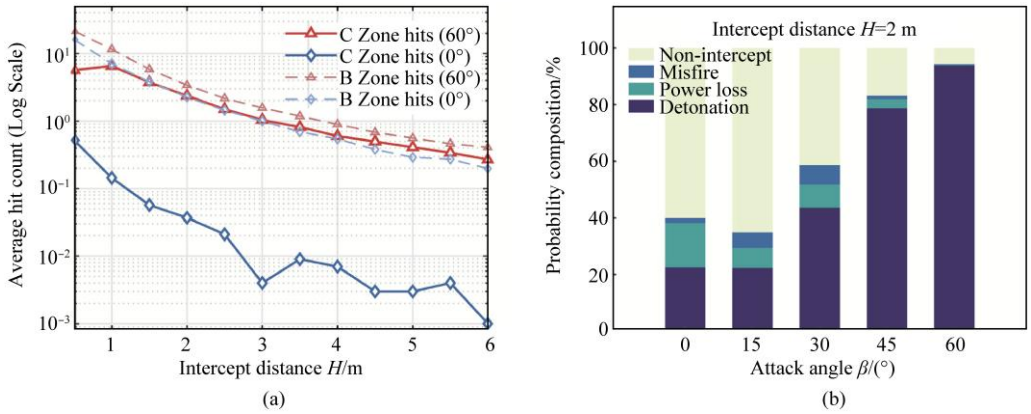

Fig. 29. Mechanism of attack angle on damage probability. (a) Number of fragment hits in key zones under different attack angles; (b) Evolution of damage mode composition for H = 2 m.

Differences in the number of fragment hits across various zones lead to changes in the composition of the rocket's damage modes (H = 2 m), as shown in Fig. 29(b). At $\beta = 0°$, the "Power Loss" mode accounts for a significant portion (15.6%). Contrary to the general rising trend, a minimum in probability appears at $\beta = 15°$. The total damage probability is actually lower than that at $\beta = 0°$. This occurs because the slight increase in attack angle makes it more difficult for fragments to meet the criteria for Zone *B*. Meanwhile, fragments are insufficient to hit the Zone *C* due to the occlusion. As $\beta \geq 30°$, the increasing inability of fragments to satisfy Zone *B* criteria results in the gradual disappearance of the "Power Loss" mode. Meanwhile, fragment impacts on Zone *C* leads to a growing probability of "Detonation" mode. Given that " Premature Detonation " is the primary damage mode, for optimal interception probability, it is advisable to keep the value of the attack angle greater than $30°$.

While the specific quantitative boundaries (such as the 90% near-field probability range) derived in this section are inherently tied to the structural layout and damage criteria of the selected rocket, the overarching "Launch–Flight–Encounter–Damage" assessment methodology possesses extensive generality. The proposed framework can be readily adapted to evaluate various fragment-based interceptor against different munition types. Furthermore, for other rockets or missiles sharing a similar functional layout, the macroscopic interception mechanisms revealed here—such as the transition of damage modes at large attack angles—exhibit highly consistent qualitative trends. Therefore, these mechanisms provide valuable theoretical references for the optimization of APS.

6.Conclusions

This study establishes a comprehensive, multi-zone damage assessment framework for rockets intercepted

by fragment cloud, integrating localized damage criteria with a high-efficiency intersection algorithm. By transitioning from traditional empirical models to component-level damage physics and optimizing the geometric encounter calculation, the main conclusions and innovations are summarized as follows:

(1) Quantified multi-zone damage criteria: The critical velocity for the piezoelectric fuse was determined to be 4 m/s. The effective velocity range for liner failure was derived as 1100–1800 m/s, the angular range is quantified by Eq. (7). Furthermore, a continuous critical velocity surface for the charge shock initiation was constructed, providing a rigorous quantitative basis for determining damage modes.

(2) An optimized projectile-target intersection algorithm: A high-efficiency "Point-to-Surface Distance Method with an Enclosing Shell" was proposed. By integrating cylindrical enclosing shell pre-filtering with a coarse/fine time-step strategy, this innovation enables large-scale statistical simulations for encounter parameter calculation to be executed rapidly without sacrificing geometric precision.

(3) Interception mechanisms and engineering implications: The damage probability remains extremely high in the near-field. As the intercept distance increases, at large attack angles, more fragments strike the charge, driving a transition in damage mode from "Loss of Warhead" to "Premature Detonation". This advantage extends the 50% probability threshold from 1.3 m to 3.7 m, a nearly threefold increase. These findings demonstrate that enforcing large attack angles is a critical strategy for maximizing the effective defensive perimeter at extended ranges.

Declaration of competing interest

The authors declare that they have no known competing financial interests or personal relationships that could have appeared to influence the work reported in this paper.

Acknowledgements

The reported research is supported by the National Natural Science Foundation of China (Grant No. 12372361).

References

[1] Rottman GL. The Rocket Propelled Grenade. London: Bloomsbury Publishing, 2011.

[2] Yang LK, Xu JG. Analysis on the development of active protection system for tanks and armored vehicles. J Phys: Conf Ser, 2021; 1855(1):012034.

[3] Ren XG. Foreign tank armored vehicle active protection system introduction. Fire Control Command Control, 2010; 35(S1):4–6.

[4] Wang S, Ma F, Guo X. Damage assessment of ordinary weapons. Beijing: Beijing Institute of Technology Press, 2021.

[5] Wang Y, Zhang B, Tang K, et al. Vulnerability Equivalent Structure Modeling and Damage Law Analysis Method for Complex System Target. Journal of Projectiles, Rockets, Missiles and Guidance, 2019; 39(5): 99-102.

[6] Goodrum CJ, Shields CPF, Singer DJ. Understanding cascading failures through a vulnerability analysis of interdependent ship-centric distributed systems using networks. Ocean Eng, 2018; 150:36–47.
[7] Cao Y. The combination of fault tree analysis and weapon effects simulation in target vulnerability research M.E. ChangSha: National University of Defense Technology, 2016.
[8] Wu J P, Song P, Hao C B, et al. Simulation of measuring method for space-time distributed parameters of multiple projectiles. Binggong Xuebao/Acta Armamentarii, 2015; 36(10): 1967-1974.
[9] Li, Y, Liu, X. Research on Damage Effect Calculate of Random Figure Face Target. Fire Control and Command Control, 2008; 33: 141-142.
[10] Zhu, L, Wen, S, and Li, Z. Research on proximity damage modeling in multiple attitude missile-target encounter. Foreign Electronic Measurement Technology, 2019; 38(10): 30-33.
[11] Lomazzi L, Cadini F, Giglio M, Manes A. Vulnerability assessment to projectiles: approach definition and application to helicopter platforms. Def Technol, 2022; 18(9): 1523–37.
[12] Li H S, Zhang X Q, Gao J C. A cloud model target damage effectiveness assessment algorithm based on spatio-temporal sequence finite multilayer fragments dispersion. Def Technol, 2024; 40:48–64.
[13] Felix D, Colwill I, Stipidis E. Real-time calculation of fragment velocity for cylindrical warheads. Def Technol, 2019; 15(3):264–71.
[14] Liu J. Simulation Research on the Interception Probability of the Flynet Active Protection System. Nanjing University of Science and Technology, 2021: 54-57.
[15] Li JW.Research on intercept probability of tank active protection system using hard kill mode. Xidian University, 2014: 43-48.
[16] Yu B, Li X, Lu F. Fast vulnerability analysis method of missile sections under the attack of fragment, J. Ordnance Equip. Eng, 2020; 41(12): 82-86.
[17] Liu YM, Xiong ZM, Wang J, Wang DR. Monte Carlo-based analysis and experimental validation of the interception-damage probability of the new active interception net. Math Probl Eng, 2022: 5438023.
[18] Fayed AIH, Abo El Amaim YA, Elgohary DH. Investigating the behavior of manufactured rocket propelled grenade (RPG) armour net screens from different types of high performance fibers. International Journal of Science and Research, 2019; 8(5): 2088-2091
[19] Żochowski P, Warchoł R. Experimental and numerical study on the influence of shaped charge liner cavity filing on jet penetration characteristics in steel targets. Def Technol, 2023; 23:60–74.
[20] Hafizoglu H, Konokman HE, Kesemen L, Atay AK. Effect of fragment impact on shaped charge jet formation and penetration into steel target. World J Eng, 2023; 20(3): 577–90.
[21] Chanteret P Y. Effect of fragment impact on shaped charge functioning[C]//19th International Symposium on Ballistics. Interlaken, 2001.
[22] Cao H. Factors Influencing the Initiation and Instantaneity of Piezoelectric Fuzes. Acta Armamentarii, 1979: 154-166.
[23] Ma YM, Tang K, Hou YK, Gong HX, Gu MH, Wang JR, et al. Experimental and numerical investigation on the oblique penetration of jacketed long-rod projectiles into spaced targets. Int J Impact Eng, 2025; 206:105463.
[24] Li CL. Experimental Investigation into the Constitutive Relationship of 2A12 Aluminum Alloy. Harbin Institute of Technology, 2006: 40-42.
[25] Zu XD, Huang ZX, Jia X. Study on rubber composite armor anti-shaped charge jet penetration. Propellants Explo Pyrotec, 2013; 38(5): 695–702.
[26] Liu P, Wang YS, Wen Q, Zhang ZB. Approximate analytical expression of supersonic projectile low trajectory. J Detect Control, 2016; 38(1): 18–23.
[27] Zhang JP, Wang YS, Li ZH, Wen Q, Zhang ZB. Buckling characteristics simulation of cylindrical support under dynamic load. J Detect Control 2016; 38(2): 37–42.

[28.] Urtiew PA, Vandersall KS, Tarver CM, Garcia F, Forbes JW. Shock initiation of composition B and C-4 explosives: experiments and modeling. Russ J Phys Chem B 2008; 2(2): 162–71.
[29] Wang SS, Li CJ, Ma XF, Sui SY. An experimental study on the initiation of covered charge impacted by tungsten alloy fragments. Acta Armamentarii 2001; 22(2): 189–91.
[30] Luo WH, Yang JJ. Study of the Main Coordinate Systems and Conversion in the KKV Simulation System. Journal of Projectiles, Rockets, Missiles and Guidance, 2007; 27(5): 289-292.
[31] Li HS, Zhang XQ. A target damage effectiveness assessment mathematical calculation method with uncertain information based on an adaptive fuzzy neural network. Int J Intell Syst 2023, 2023: 9330296.
[32] Chen X. Research on shock initiation of charged structure by shock waves and high-velocity fragments.Nanjing University of Science and Technology, 2023: 59-78.

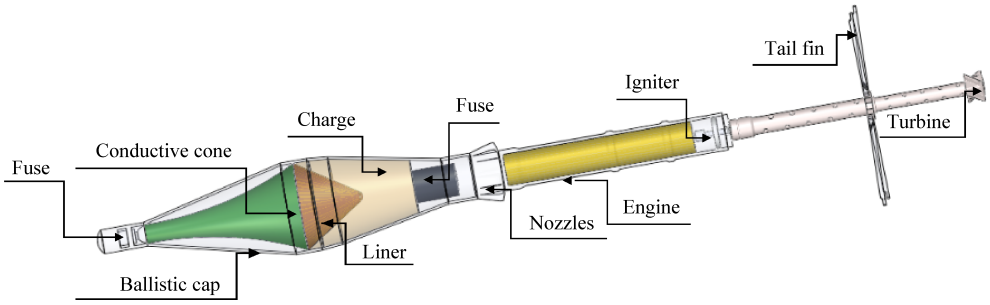

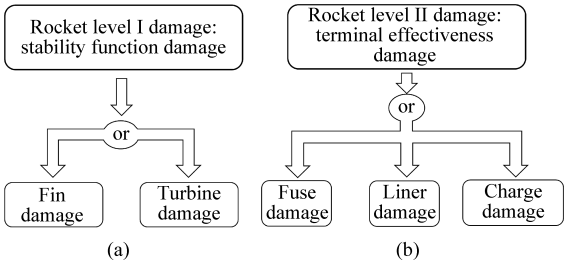

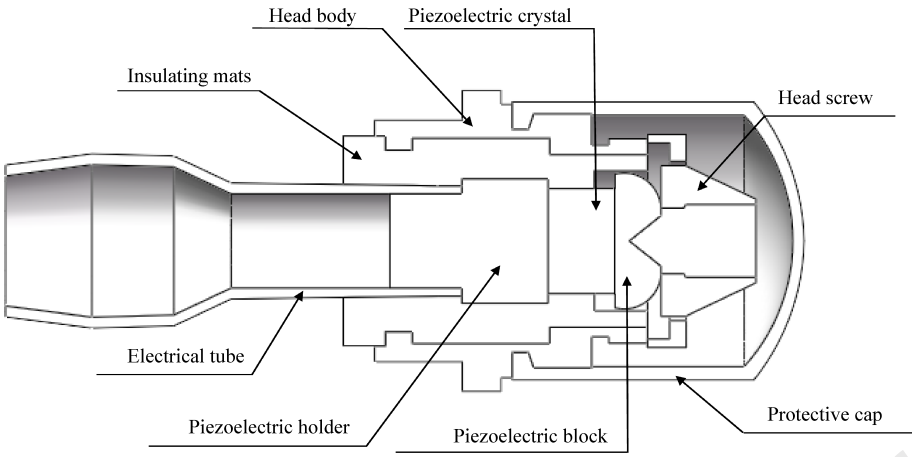

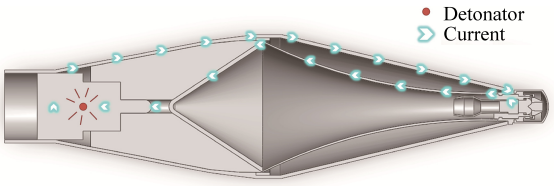

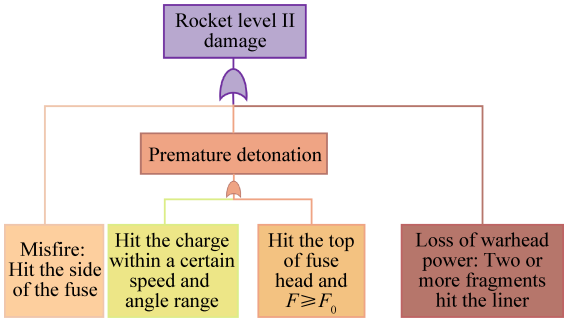

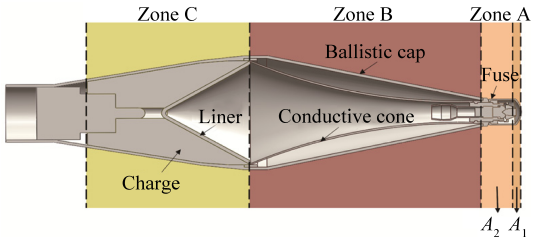

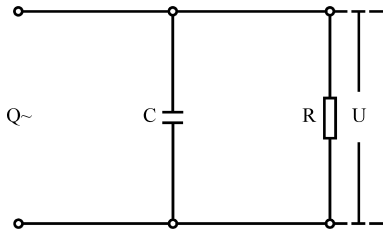

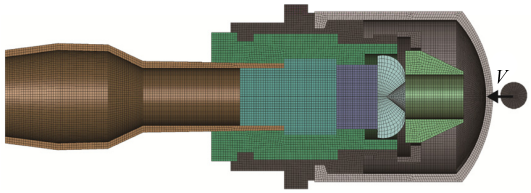

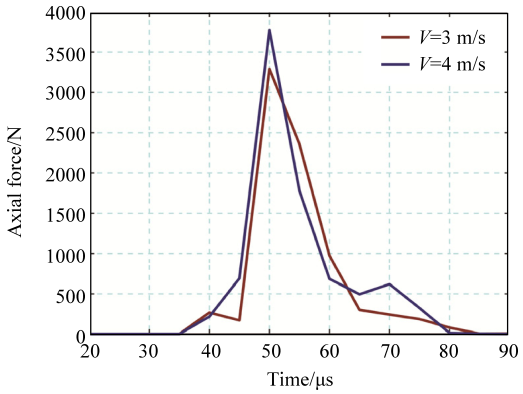

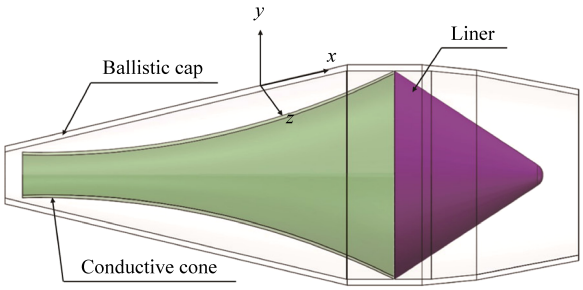

(a)

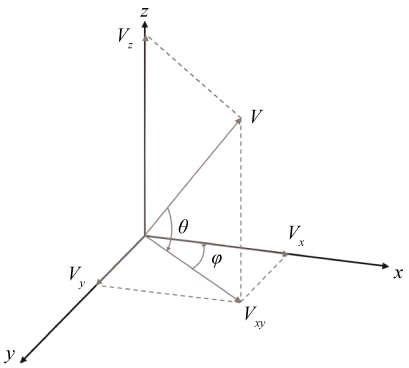

(b)

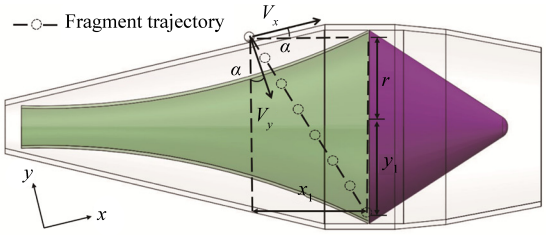

(a)

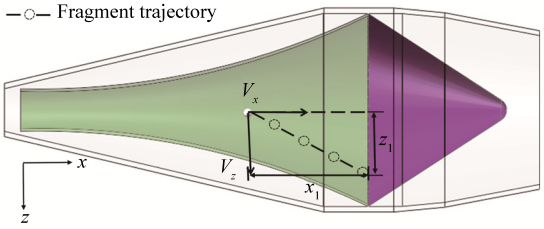

(b)

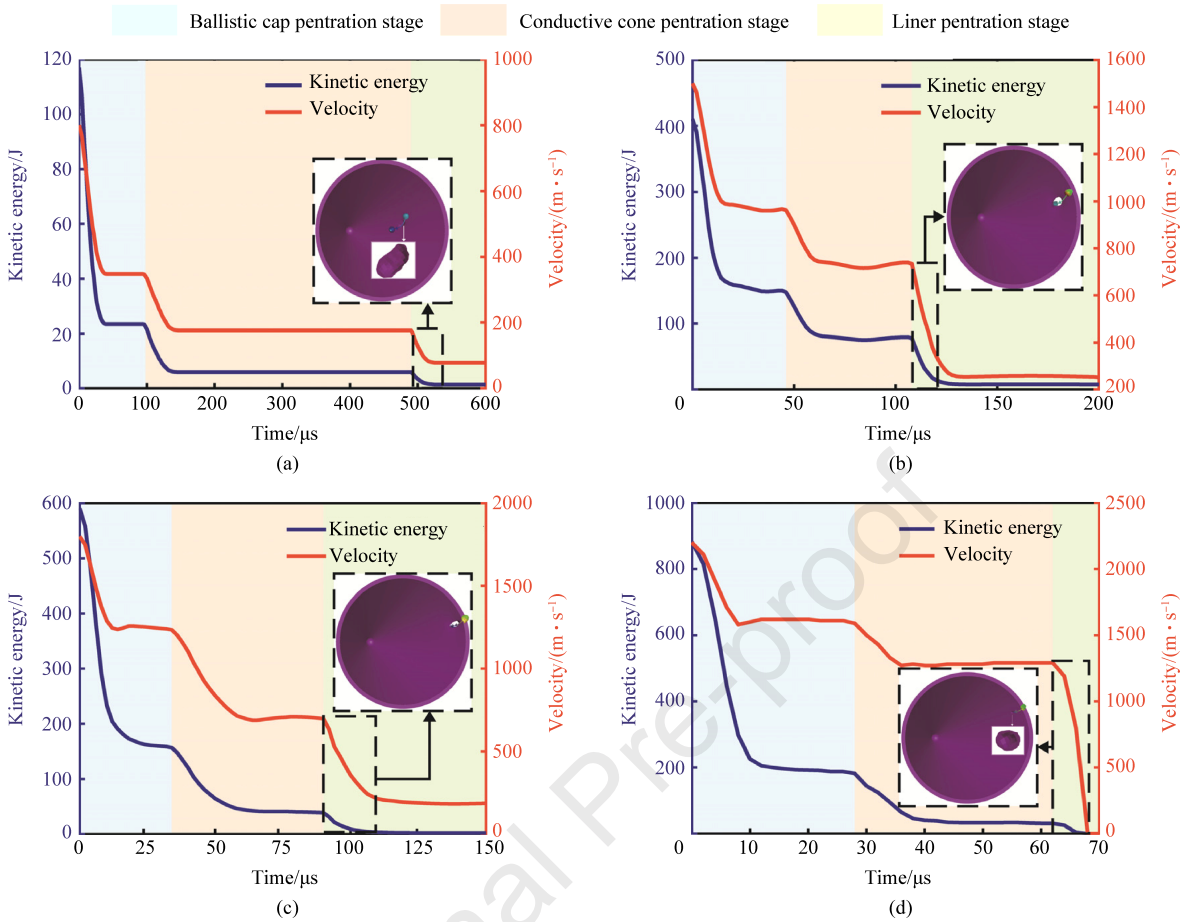

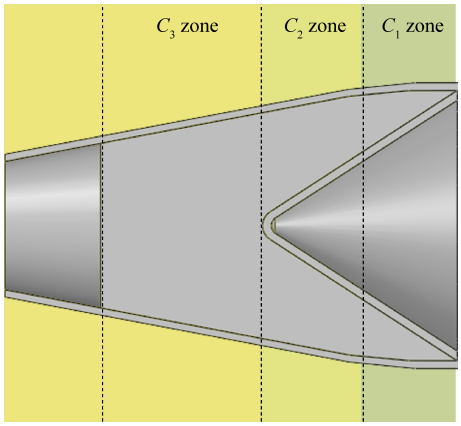

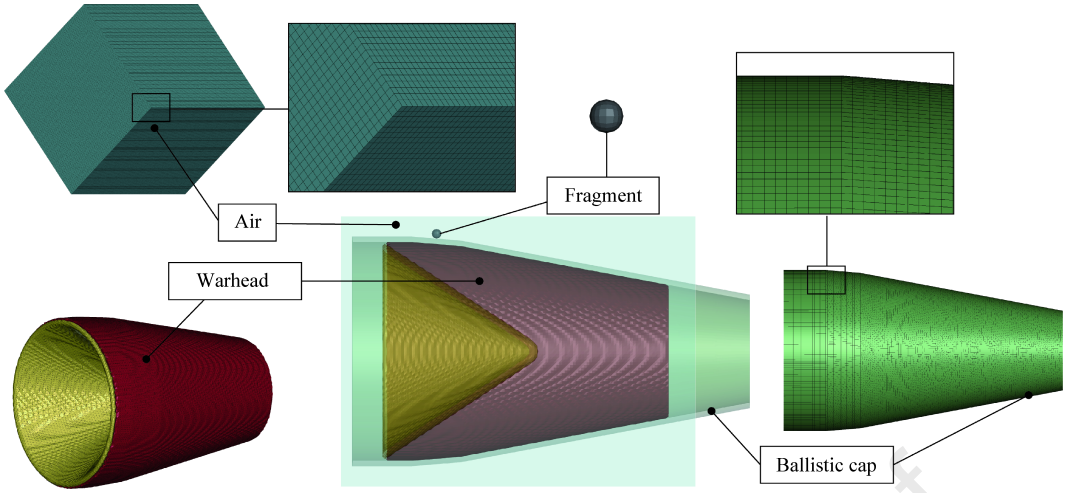

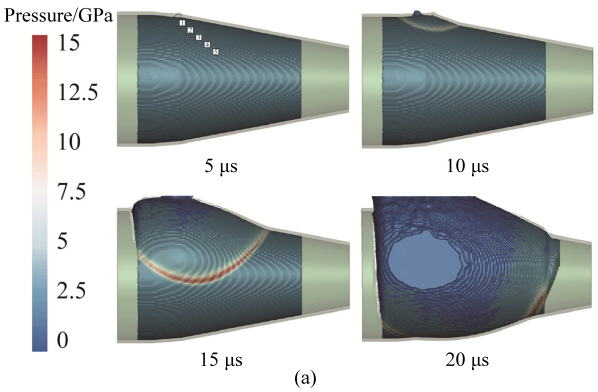

(a)

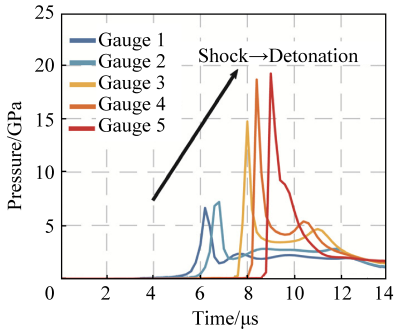

(b)

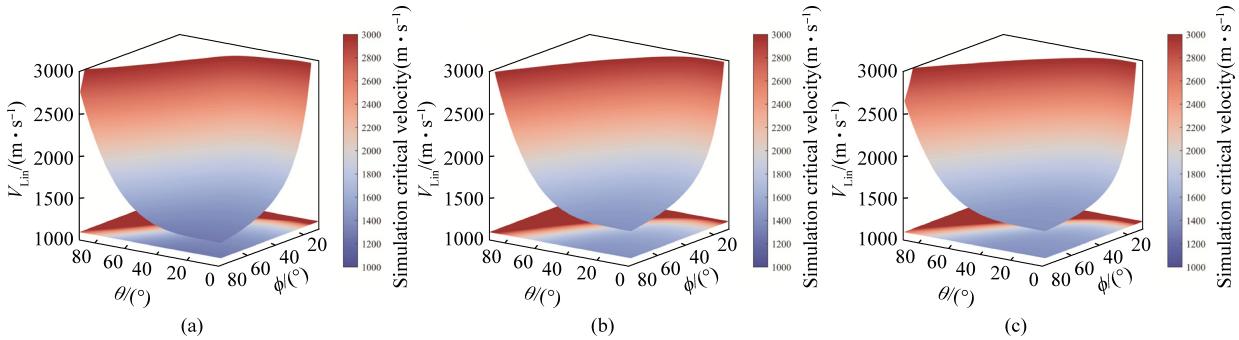

(a) (b) (c)

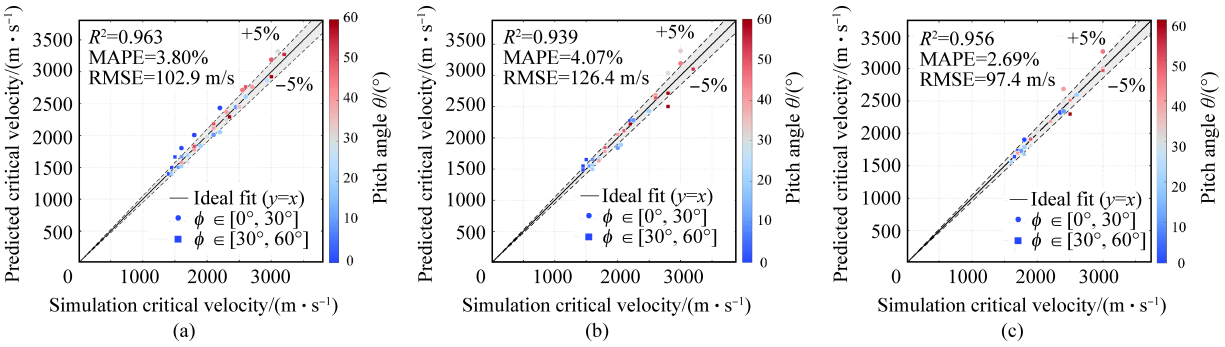

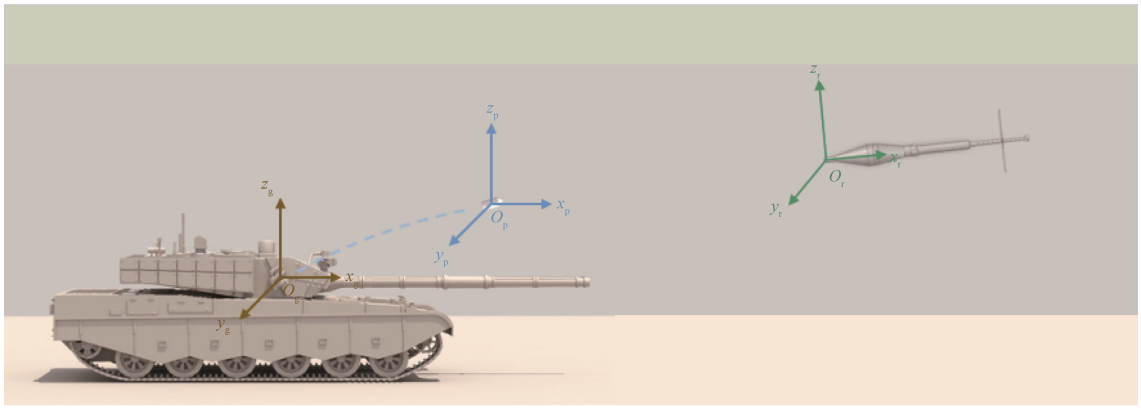

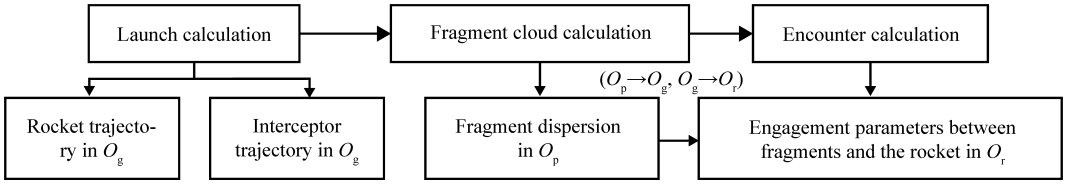

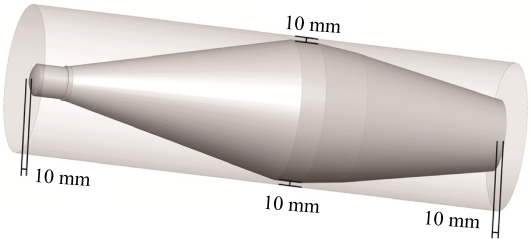

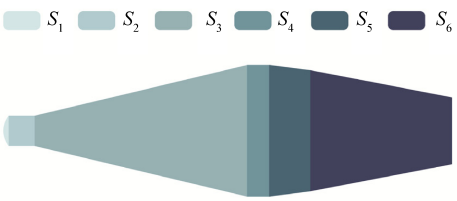

(a)

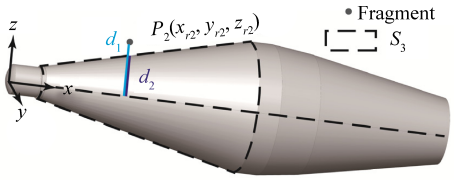

(b)

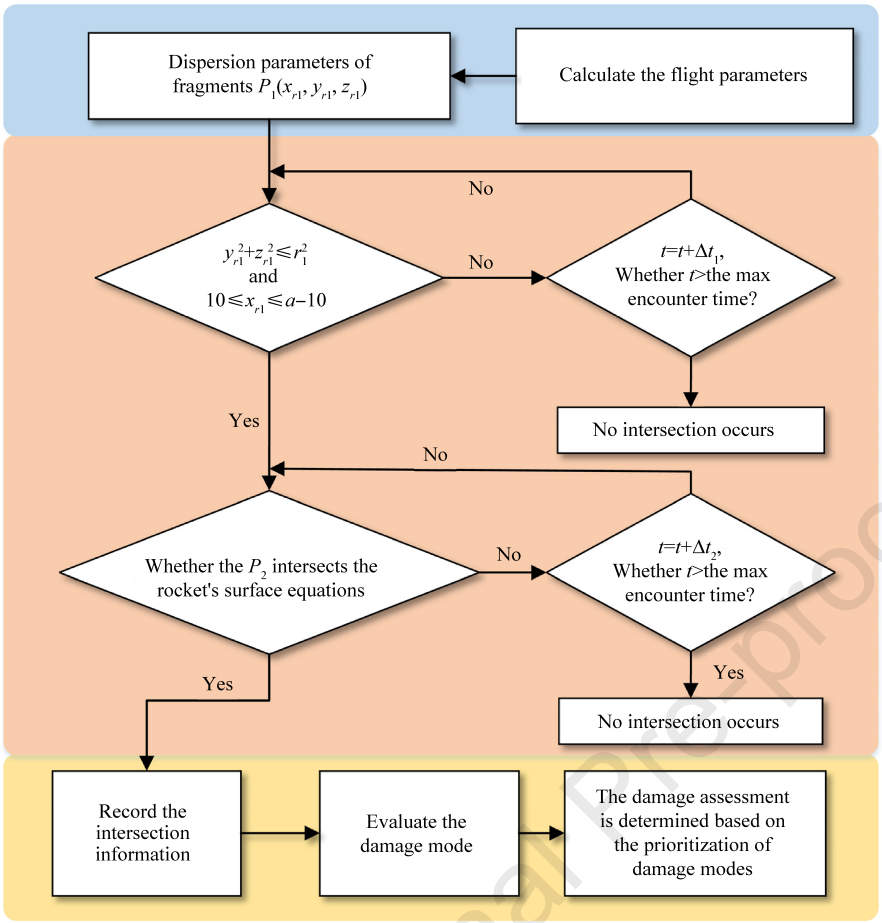

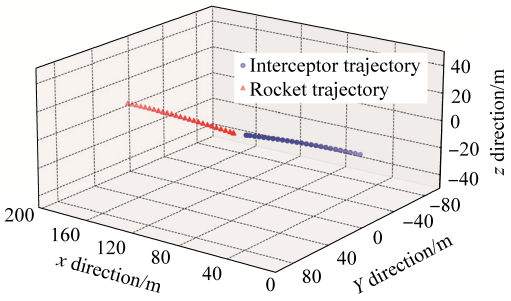

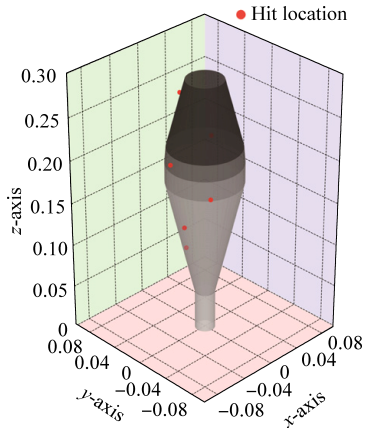

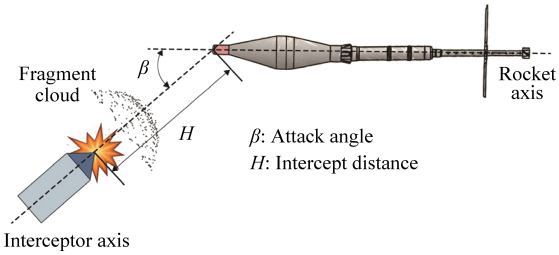

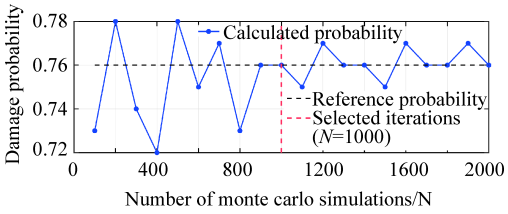

(a)

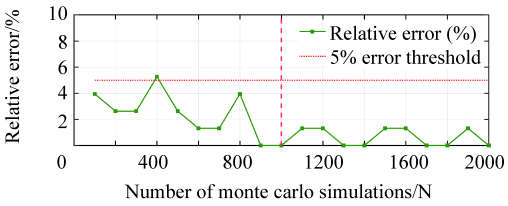

(b)

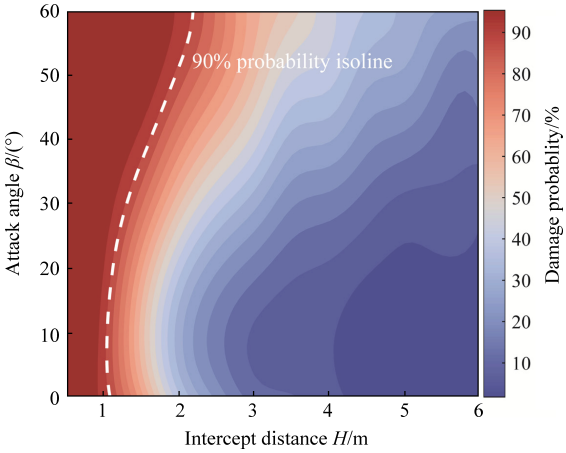

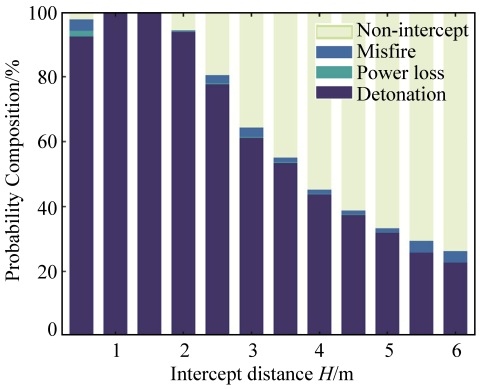

(a)

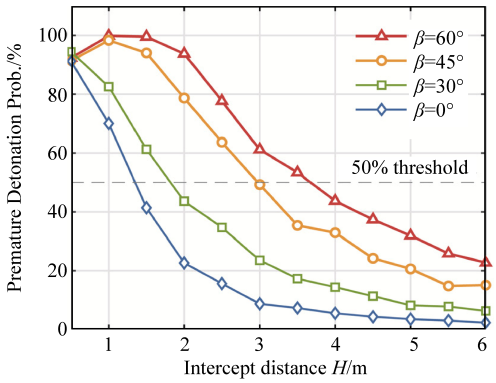

(b)

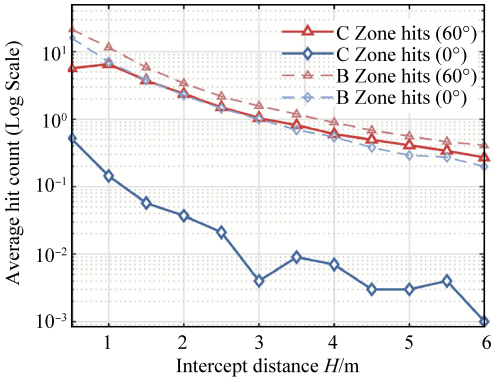

(a)

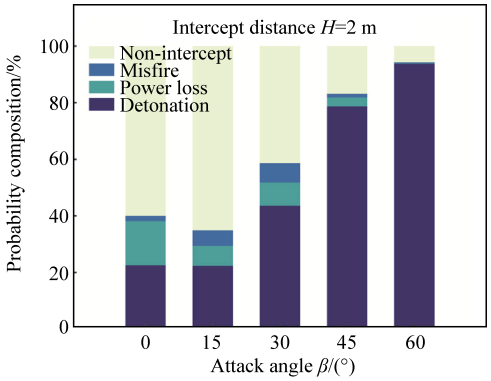

(b)

Declaration of Interest Statement

☒ The authors declare that they have no known competing financial interests or personal relationships that could have appeared to influence the work reported in this paper.

☐ The author is an Editorial Board Member/Editor-in-Chief/Associate Editor/Guest Editor for this journal and was not involved in the editorial review or the decision to publish this article.

☐ The authors declare the following financial interests/personal relationships which may be considered as potential competing interests: